Fluorophore interactions with the surface modes and internal modes of a photonic crystal

Fluorophore interactions with the surface modes and internal modes of a photonic crystal / Badugu, R.; Blair, S.; Descrovi, E.; Lakowicz, J. R.. - In: OPTICAL MATERIALS. - ISSN 0925-3467. - 147:(2024), pp. 1-12. [10.1016/j.optmat.2023.114718]

Publisher:
Elsevier

Published
DOI:10.1016/j.optmat.2023.114718

Fluorophore Interactions with the Surface Modes and Internal Modes of a Photonic Crystal

Ramachandram Badugu[1], Steve Blair[2], Emiliano Descrovi[3], and Joseph R. Lakowicz[1]

[1]Center for Fluorescence Spectroscopy, Department of Biochemistry and Molecular Biology, University of Maryland School of Medicine, Baltimore, MD 21201, United States.

[2]Department of Electrical and Computer Engineering, University of Utah, 50 South Central Campus Drive, Room 2110, Salt Lake City, UT 84112, United States

[3]Department of Applied Science and Technology, Polytechnic University of Turin, corso Duca degli Abruzzi 24, 10129 Turin, Italy

Highlights

- The emission spectra of Ru probe were measured when placed on top of a 1DPC.
- The S-polarized coupled emission spectra of Ru probe on 1DPC exhibits two are more peaks and their maxima shift to shorter wavelengths with increasing observation angle.
- The two intense S-polarized Ru probe emission band peaks results from emission coupling to the BSW and first internal mode of the 1DPC.
- Finite-Difference Time-Domain (FDTD) simulations were performed to confirm fluorophore coupling to the BSW and internal modes.
- Simulated results are in excellent agreement with the experimental data.

Figure for Graphical Abstract

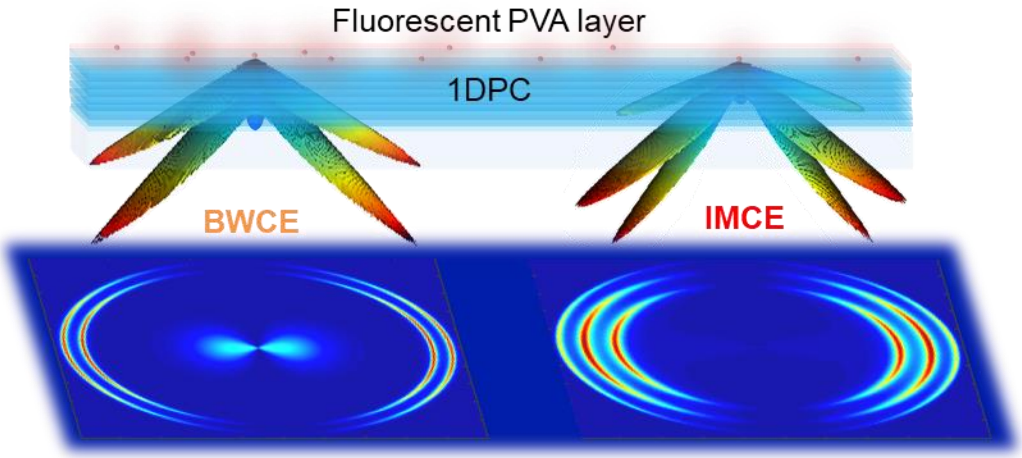

Abstract

The metal-ligand complex tris(2,2'-bipyridine)ruthenium(II) chloride (Ru probe) displays a broad emission spectrum ranging from 540 to 730 nm. The emission spectra of Ru probe were measured when placed on top of a one-dimensional photonic crystal (1DPC), which supports both Bloch surface wave (BSW) and internal modes for wavelengths below 640 nm and only internal modes above 640 nm. The S-polarized emission spectra, with the electric vector parallel to the 1DPC surface, were found to be strongly dependent on the observation angle through the coupling prism. Also, the usual single broad-emission spectrum of Ru probe on glass was converted into two or more narrow-band-spectrum on the 1DPC, with emission band maxima dependent on the observation angle. The two S-polarized emission band peaks for Ru probe were found to be consistent with coupling to the BSW and first internal mode (IM1) of the 1DPC. The same spectral shifts and changes in emission maxima were observed by using Kretschmann and reverse Kretschmann illuminations. As the coupling requires the emitter to be in proximity with the photonic structure, we calculated near- and far-field distributions of a dipole directly located on the 1DPC surface. Finite-Difference Time-Domain (FDTD) simulations were performed to confirm fluorophore coupling to the BSW and internal modes (IMs). Both the measured and simulated results showed that IM coupled emission is significant. Coupling to the IM mode occurred at longer wavelengths where the 1DPC did not support a BSW. These results demonstrate that a simple Bragg grating, without a BSW mode, can be used for detection of surface-bound fluorophores.

Keywords: One-dimensional photonic crystals; Optical modes; Bloch surface waves; Bloch surface wave-coupled emission; Internal mode coupled emission; Bragg gratings; Finite-Difference Time-Domain.

Introduction

Fluorescence detection and spectroscopy have made significant contributions to biophysical and biomedical research for the past 60 years [1]. During these years there have been advances in time-resolved instrumentation [2], fluorescent probe chemistry [3,4], microwell plate readers [5] and fluorescence microscopy [6,7]. These diverse instruments and measurements share a common feature, which is collection and detection of free-space emission propagating through lenses, filters, objectives, and monochromators, each of which decreases the amount of radiation power that is reaching the detector. Additionally, emission often occurs almost uniformly in all directions, and it is difficult to capture more than a small fraction of the total emission. Stated alternatively, we have accepted what nature provides for far-field dipole radiation into a medium of constant or nearly isotropic photonic mode density (PMD) or optical density-of-states (DoS), and then use external optical components to collect and select the desired emission.

About twenty years ago, researchers began to question if free-space emission spectral properties of fluorophores could be changed by close-proximity of plasmonic structures. Such changes seemed possible because of the unusual photonic density-of-states near metallic structures. Measurement of near-field effects on fluorophores started with the use of metallic nanoparticles to modify the rates of absorption and emission [8,9]. The optical cross-sections for metallic nanoparticles can be many-fold larger than those physical sizes which results in enhanced local fields for excitation of fluorophores [10,11]. The high density-of-states near the metal particles can increase the rate of emission [12,13]. These effects on excitation and emission do not require fluorophore-metal contact and are due to through-space, near-field interactions of the fluorophores with metallic particles. These effects of metallic particles are now widely used in fluorescence sensing [14-16]. Metal-enhanced fluorescence (MEF) is limited to a few noble metals, which support surface plasmons and requires surface chemistry to keep the fluorophores more than 10 nm from the surface to avoid the quenching effect.

Another important advancement was the discovery of directional emission from fluorophores on thin metal films. Emission from fluorophores on continuous gold, silver, or aluminum films of 20 to 50 nm thick, can couple with surface plasmons which then radiate into the substrate at a specific angle controlled by the optical constants of the metal films. This phenomenon is called surface-plasmon coupled emission (SPCE). For a smooth metal film there is a cone-of-emission at the plasmonic resonance angle for that emission wavelength [17,18]. More complex emission spatial distributions can be observed with gratings or concentric circular structures [19,20].

Photonic crystals (PCs), which do not contain any metals, can also modify the local density-of-states (LDoS) and can be expected to modify the emission from excited state fluorophores. PCs display unique optical properties because some light frequencies can penetrate the structures and other frequencies cannot propagate within the crystal, resulting photonic band gaps (PBG) [21-24]. In contrast to metallic structures discussed above, the optical properties of dielectric photonic crystals can be changed to the wavelengths of interest by changing the dimension of constituting layers. Much of the early research was performed using two-dimensional (2D) or three-dimensional crystals (3D). A 2D photonic crystal can be a regular array of cylinders with a refractive index different than the surrounding volume, and dimensions comparable to the wavelengths of interest. An example of a 3D photonic crystal is a regular array of dielectric spheres in an opal-like structure. Because excited state fluorophores behave like radiating dipoles a PC that alters the LDoS and is expected to affect the emission wavelength or decay rates of nearby fluorophores. Several reports have examined the far-field emission from fluorophores near 2DPCs and have described changes in emission spectra and the decay rates [25-27]. Additionally, emission spectra and decay rate changes have been reported for fluorophores near 3DPCs [28-30]. These results can be difficult to interpret for several reasons. The photonic band structures of 2DPCs and 3DPCs are very complex. As a result, it is difficult to correlate the far-field emission observed at a particular angle with a single mode in the photonic structure. Several groups have reported changes in the emission spectral shape of fluorophores due to PCs [31-34]. These changes could be due to optical filtering by the PC, or due to redistribution of the fluorophore emission spectrum by PCs. However even with modern lithographic techniques, it is difficult to fabricate 2D and 3D photonic crystals over a large area or for a large volume. Some structures can be made using bottom-up methods such as self-assembly, chemical etching or block copolymer lithography [35-37]. However, it is difficult to use 2D and 3DPCs for biomedical sensing because the structure needs to be permeable to the sample. The wide range of solution compositions used in chemical sensing can change the dimensions of the 2D and 3D photonic crystals [38,39]. Additionally, the PBG can prevent light from entering or exiting the structure.

In the present paper we describe the interactions of fluorophores with a one-dimensional photonic crystal (1DPC), which consists stack of multiple thin layers of two dielectrics with different optical constants and thicknesses. 1DPCs do not contain nanoscale features in the x-y plane and can be fabricated with simple vapor-deposition, physical sputtering, or spin-coating methods, which simplifies the fabrication of structures with large area. Additionally, the optical modes of a 1DPC are much simpler than the 2D or 3D structures, which greatly facilitates the selection of angles for measurement and interpretation of the angle-dependent emission spectra. The number of available optical modes can be small, which facilitates the detection of mode-coupled far-field radiation according to specific angular and spectral dispersions. For example, coupled emission can be observed at different angles, relative to the surface normal (z) of the multilayer. The optical modes in a 1DPC are characterized by electric fields mainly localized inside the structure or confined close to the surface. The surface-bound modes are called Bloch surface waves (BSW), whose intensity can be strongly enhanced relative to the incident field because of low optical losses within dielectrics. Accordingly, the emission from fluorophores on the surface of a 1DPC can couple with surface modes and display BSW-coupled emission (BWCE) [40-42]. Emission coupling to internal modes (IM) can also occur, despite their low intensity and that are typically buried within the 1DPC and result internal mode couped emission (IMCE). The occurrence of internal mode coupled emission has been noticed in previous reports but was not investigated in detail [41,42].

Many modern fluorophores have narrow absorption and emission spectra, which can make it difficult to observe both BWCE and IMCE from the same fluorophore. For this reason, we selected tris(2,2'-bipyridine)ruthenium (II) chloride, hereafter called the Ru probe, which displays a broad emission spectrum that could overlap with the dispersions of both the BSW and internal modes of the same 1DPC. Additionally, it is well known that fluorophore coupling also depends on the orientation of the probe transition moments relative to the mode polarization of the structure, and most organic fluorophores have unique and well-defined transition moments. This effect is minimized with Ru probe because of its symmetry and rapid redistribution of the excited state energy to the three differently oriented 2,2'-bipyridine ligands. As a result, Ru probe displays low emission anisotropy even when immobile in frozen solution [43]. In the present report we show that IMCE can have intensities which are comparable to the emission coupled with a surface mode, BSW. Internal modes exist for any regular sequence of different dielectric layers, whereas a BSW structure may need to have a defined termination layer. Therefore, simple 1D Bragg multilayers can be useful for high-efficiency detection of surface-bound fluorophores, even if BSW are not supported.

The present paper is organized as follows. The first section includes the experimental results on the emission spectra of Ru probe when placed on a 1DPC within a thin polymer film. This section shows the normally broad emission spectrum of Ru probe is converted into emission spectrum with two or more narrow emission bands. The angle-dependent emission bands were found to be consistent with the dispersion diagram of surface and internal modes calculated for the structure. We note here that, while a dispersion diagram is generally extracted from a calculated reflectivity map, wherein an incident far-field light is incident onto the 1DPC, the measured coupled emission is due to a short-range interaction between the fluorophore and the photonic structure. In order to give an account for such interaction, the second section presents Finite-Difference Time-Domain (FDTD) simulations of dipole emission from a fluorophore placed 5 nm above the top of the 1DPC. These simulations of coupled emission spectra are in excellent agreement with the experimental results. The last section describes our conclusions and some perspective on future applications of IMCE.

Materials and Methods

The fluorescent Ru probe [tris(2,2'-bipyridine)ruthenium (II) chloride, (Figure 1A)] was obtained from Sigma-Aldrich and used without further purification. Ru probe was dissolved in aqueous 1% poly-vinylalcohol (PVA) solution and spin coated on glass and on the 1DPC structure using conditions described previously to obtain a 30 nm thick PVA layer [44].

The 1DPC was made by plasma-enhanced chemical vapor deposition (PECVD) of silica (SiO_2) and silicon nitride (Si_3N_4) on standard microscope slides. This structure consisted of alternating layers of the low (L) and high (H) refractive index (n) dielectrics (Figure 1B) with seven pairs of H and L refractive index materials (H/L). The H material is 78 nm thick Si_3N_4 and the L material is 126 nm thick SiO_2. The top SiO_2 layer with 152 nm thickness was used to support a Bloch surface wave (BSW) for wavelengths below 640 nm [42]. Electric field ($|E|^2$) intensity profiles of surface and internal modes in the 1DPC were calculated using TFCalc [45]. Simulations involving emission and coupling of dipoles on the 1DPC surface were calculated using software from Lumerical, Inc [46,47]. The refractive index of SiO_2 $n_L = 1.46$ at 550 was used with a zero imaginary coefficient. To obtain a finite width of the BSW we added an imaginary component to the refractive index of Si_3N_4. The Si_3N_4 refractive index ranged from $n_H = 2.196 + i0.033$ at 550 nm to $n_H = 2.144 + i0.016$ at 633 nm [42]. The refractive indices of PVA and prism of 1.46 and 1.50 at 550 nm, respectively, were used for the calculations.

The experimental geometry and polarization conditions used for the present study are moderately complex and are shown in detail in Figure S1. The 1DPC is mounted on a hemicylindrical prism and optically coupled with index matching fluid, glycerol, to avoid total internal reflection (TIR) at the slide-prism interface. This allows light above the glass-air critical angle of the prism to enter the 1DPC and create an evanescent field near the top SiO_2-PVA layers. The prism also allows the coupled emission from above the critical angle to exit the prism and be measured in the far-field. The z-axis is the laboratory vertical axis. The incident light can reach the sample from both sides of the prism. The incident light for excitation through the prism is known as the Kretschmann (KR) configuration, and from the air-side of the sample is known as the reverse Kretschmann (RK) configuration. The results depicted in the main text were obtained using the KR configuration with an angle of incidence of 48° which was found to yield the highest emission intensity. Similar results were obtained with RK illumination and are shown in the Supplemental Material. Unless stated otherwise the excitation and emission were S-polarized, for which the electric field is perpendicular to the plane of incidence (also referred to as scattering plane) and parallel to the surface of the 1DPC. For these measurements the excitation and emission polarizers aligned with the vertical z-axis. The P-polarized emission, presented in the Supplemental Material, was measured with the emission polarizer in the horizontal orientation. As the S-polarized illumination was laboratory vertical, we also refer to S as vertically (V) polarized and P as horizontally (H) polarized.

Excitation was achieved from a CW 470 nm laser source. Emission was measured over a range of angles using a fiber optic bundle. Emission was measured on the prism side from 0 to 90°, and from the air side (free space) from 90 to 180° (Figure S1). The hemicylindrical prism has a diameter of 23 mm with a refractive index of 1.50 at 550 nm. The end of the observation fiber bundle with an aperture diameter of 1 mm, was placed 16.5 mm away from the prism surface or about 29 mm from the illuminated spot. A 500 nm long-pass filter was placed right before the fiber head to remove incident laser light. The emission passing through the fiber was measured with an Ocean Optics Flame Miniature Spectrometer. We noticed the Ru probe emission spectra measured with the Ocean Optics displayed some minor structure (Figure 2C), which was not seen with a PicoQuant MicroTime 300 spectrofluorometer. Although, this discrepancy in spectral shape does not affect our conclusions but might be due to the less-sensitive Ocean Optics instrument compared to the PicoQuant 300 instrument.

Results and Discussion

Effects of a 1DPC on Ru Probe Emission Spectra. Modes in a 1DPC are polarized relative to the surface layers of the structure. Fluorescence emission is also polarized because optical transitions have discrete directions in the molecular framework. We have minimized the impact of fluorophore's intrinsic polarization on mode coupling by using Ru probe with high symmetry and low anisotropy [43]. Therefore, the polarization of the emitted radiation will mainly be due to the 1DPC, with only a minor or no contribution from the fluorophore's orientation. Calculated reflectance spectra of the 1DPC at various angles of incidence are presented in Figure 2A, which shows modest agreement with the measured apparent absorption spectra (Figure 2B). We use the term "apparent absorption" because the optical density includes the effects of absorbance and reflectance. The high apparent absorption at 670 nm and 0° incidence is due to the PBG which reflects light at this wavelength (Figure 2B). As expected from Bragg gratings, the PBG shifts to shorter wavelengths as the angle of incidence increases (Figure 2B). Depending on the observation angle, the wide emission spectra of Ru probe on a glass slide overlaps either side of the PBG of the 1DPC as shown in Figure 2C, which compares the S-polarized coupled emission (CE) spectra of Ru probe on the 1DPC with an observation angle of 47°. Such dramatically altered emission spectra were reported previously [31-34], and some spectral changes were explained by invoking a redistribution of the emission due to the 1DPC.

Angle-dependent emission intensities were measured for the Ru probe on the 1DPC structure (Figure 3A) using KR excitation, and both the S- and P- polarized emission were observed. The S-polarized emission at 600 nm was highly constrained around an angle of 44.5° which was assumed to be Bloch surface wave-coupled emission (BWCE). An additional smaller intensity peak was observed near 63.5°. A similar angular intensity distribution, with about 2-fold weaker intensity, was observed with RK excitation (Figure S2). This observation indicates that the emission angle is independent on how the excitation is performed. This near independence from the mode of excitation will simplify the use of 1DPCs in microplate readers or point-of-care sensing devices. Emission through the coupling prism was not completely S-polarized. Some P-polarized emission was also observed (Figure 3B), which is about 5-fold weaker than S-polarized emission. The angular distribution of the P-polarized emission was comparable to that observed on a plain glass slide (Figure 3C).

The emission was measured in ranges of angles and to simplify we divided these angles into two ranges, Range 1 from 43 to 49°, and Range 2 from 52 to 73° (Figures 4A and 4B, respectively). These angle-dependent spectra showed two widely separated peaks in both angular ranges. Similar spectra were observed with RK excitation (Figures S3A and S3B). These usual spectra were observed for Ru probe on glass and the emission was distributed over a wide range of angles (Figures 4C and S3C). The origin of the multiple peaks was clarified by separated plotting of the normalized emission spectra at each observation angle (Figure 5). These spectra reveal a systematic blue-shift of the BSW-coupled emission and the appearance of a new optical mode-coupled emission which also consistently moves to shorter wavelengths with larger observation angles. Once again, similar results were observed with RK excitation (Figure S4). The angle-dependent spectral maxima were found to be in good agreement with the angularly- and spectrally-resolved reflectivity diagram calculated for the 1DPC illuminated from the glass substrate (Figure 6 and Figure S5). The emission maxima in Range 1 are consistent with coupling to the BSW mode. The emission maxima at larger observation angles are consistent with coupling to internal mode 1 (IM1) or internal mode 2 (IM2).

P-polarized coupled emission spectra are shown in Figure S6 and S7 from 42 to 76^{o} of the observation angles, respectively. Compared with S-polarized emission, P-polarized coupled emission is about 4-fold weaker and less sensitive to change in observation angle. This can be confirmed by 1DPC reflectance distribution at 600 nm in Figure 7A, where P-polarized light shows high reflectivity value across all angles above the critical angle.

More insights on the optical modes evidenced in Figure 6, which can be obtained by calculating the electric field intensities distributions ($|E|^2$) associated to specific wavelength-angle of incidence. Such intensity distributions provide good indication of the ability of emission to couple with these modes. Figure 7A shows the reflectance spectrum of the 1DPC for 600 nm KR illumination light. The narrow drop to near zero reflectance around 44^{o} is due to the BSW mode. Internal modes occur at larger angles for the same 600 nm wavelength. The incident light is enhanced near the top of the 1DPC (Figure 7B) because the structure contains only dielectrics with low optical losses.[48] For the assumed imaginary constant for Si_3N_4 the incident light intensity is enhanced near 3000-fold.

The electric field distribution and intensities are very different for light coupled to the internal modes as compared to that of BSW mode. Most of the energy carried by the internal mode labelled as IM1 is well-confined within the bulk of the 1DPC structure (Figure 7C). The highest peak intensity is about 75-fold lower for IM1 as compared to that of for BSW under the same assumption of Si_3N_4 imaginary constant. Interesting to note that the fluorophore lays several nanometers away from the IM1 maximum intensity peaks. While this distance is too large for typical fluorescence resonance energy transfer (FRET) to occur, which is also a near field effect between a donor and an acceptor molecule and rarely occurs over distances more than 10 nm [49]. A weak emission coupling with internal modes can still take place for this structure with over several microns separation between internal mode filed location and the fluorophores positioned on the surface, allowing the IMCE.

Computational Analysis of 1DPC Mode-Coupled Emission. As shown in the last section, a relatively high intensity of the IM1-coupled emission was observed for Ru probe on 1DPC. The short-range interactions of a dipole with the 1DPC were investigated using finite-difference time-domain (FDTD) simulations. We have already shown that the radiative pattern of the BWCE and IMCE are basically scaled when switching from RK to KR excitation (Figures S3 and 4, respectively). Stated otherwise, setting the illumination conditions in resonance with either the BSW or any IMs does not particularly alter the angular distribution of the emitted radiation. Our simulations focused on an excited state dipole, positioned 5 nm above the top SiO_2 layer and within the 30 nm PVA film (Figure 8). The dimensions of the simulated 1DPC were the same as shown in Figure 1. A Discrete Fourier Transforms (DFT) linear monitor along x-axis was placed just beneath the 1DPC bottom Si_3N_4 layer to collect the coupled radiation within x-z plane propagating into the glass substrate. From this field distribution, a projection algorithm provides the far-field distribution to be compared with our experimental results. From the simulations we could extract the emission intensities for any observation angle or emission wavelength. The FDTD calculation area was set as large as 80 μm x 4 μm to collect more coupled emission from the monitored spot, with another small much finer mesh cells of 5 nm x 1 nm in x-z plane. A second DFT linear field monitor was placed in x-z plane along a transverse cross-section of the 1DPC, to obtain the intensity distribution across the structure.

The FDTD method was used to calculate the field intensity ($|E|^2$) at 1 nm spectral intervals from 540 to 800 nm. The simulations were performed with a single dipole aligned along the three orthogonal orientations separately, along the x-axis parallel to the 1DPC surface, along the z-axis perpendicular to the 1DPC surface, and along y-axis parallel to the 1DPC surface but perpendicular to the x-z plane. All three orientations are expected to be relevant due to the low anisotropy of Ru probe and the complex polarization in the near-field region of a dipole [50]. The sum of the field intensity calculated from the former two simulations with the dipole oriented along x- and z- axis contributes to the electric field component of the emitted radiation polarized parallel with the plane of scattering and was termed as $|E_p|^2$, while the y-axis-oriented dipole directly provides the electric field component polarized perpendicular to the plane of incidence and was referred as $|E_s|^2$. Thus, the electric field components $|E_p|^2$ and $|E_s|^2$ calculated in the far-field correlate with the P- and S-polarized emissions in our experiments, respectively.

We simulated the near-field intensity and Poynting vector distributions for a $\vec{Y}$-oriented dipole placed 5 nm above the 1DPC so as to compare BSW and IM1 coupled emission with measured S-polarization emission. The wavelengths of 590 and 690 nm were selected because of the emission resonances of BWCE and IMCE shown in Figure 4A observed at 45° (green line). As can be seen from Figure 9A, the dipole at 590 nm induced a strong surface-localized field that can leak into the structure at a specific emission angle. Experimentally, the observed region of illuminated fluorophores on top of 1DPC was about 1 mm in diameter. In a previous publication, we showed that a BSW can propagate over 10 µm across the surface [51], and even longer propagation lengths have been reported [52,53]. Therefore, the simulations in Figure 9 underestimated the BWCE which occurs along the observation region. At 690 nm (Figure 9B) the surface BSW wave is no longer supported. Most of the emitted radiation was coupled to internal mode(s). A similar observation was observed with the Poynting vector distributions for 590 and 690 nm shown in Figures 9C and D, respectively.

Radiation leaking into the glass substrate was detected by using a linear monitor oriented along x-axis right below z = 0. Such intermediate field was then projected into far-field with angular dependence. The calculated radiative patterns are shown in Figure 10A displaying the field intensity at selected wavelengths of 595 and 685 nm. At 595 nm, three modes were present at different angles and corresponded with the BSW and IM modes shown in Figure 7A (red line), where the BWCE dominated and reached its maximum compared with the emission from the other modes. At a longer wavelength of 685 nm, the BSW is not supported, and the IM modes shifted to smaller angles. The internal modes have a wider angular width than the BSW mode, and an additional mode appeared, called IM3. In fact, the IM1-coupled emission reached its maximum value at 685 nm and the angle shifted to 44° where the BSW mode was previously dominant. This spectral overlap of BWCE and IMCE intensity maxima at different angles can be a source of confusion when measuring coupled emission, but our experiments showed BWCE and IMCE maxima can be easily resolved angularly, as shown in Figure 4A and 4B.

The calculations in Figure 10A were conducted with dipoles with equal intensities at each wavelength. However, a real fluorophore has wavelength-dependent emission intensities which will modify the coupled emission accordingly. To account for this effect, we weighed the intensities shown in Figure 10A with the free-space emission spectrum of Ru probe on a glass slide (Figure S8). The spectrum is modeled as a Gaussian weighted profile of the Ru probe emission spectra on glass (Figure S3C). We refer to these modified results as "weighted" in Figure 10B to distinguish them from the "raw" results in Figure 10A. This weighting process has a dramatic effect on the angular intensity distribution. These results also suggest that a mutli-layer structure can be designed to display higher BWCE or IMCE depending on the probe emission spectra or the layer thickness. For easy clarification, all simulation results before the weighting process were termed as “raw” results, otherwise the weighted results are presented.

To confirm our understanding of 1DPC-coupled emission, we compared the measured angle-dependent spectra (Figures 4 and 3A) with simulated spectra. First, we simulated the coupled far-field emission from a single dipole that was incrementally varied from 550 to 800 nm (Figure 11A). These “raw” spectra were then “weighted” by the Ru probe emission spectra (Figures 11B). Figure 11C shows the simulated weighted emission spectra from the larger angles. Excellent agreement was obtained for both the angle-dependent emission and intensities at all measurable wavelengths. These results make clear that dipoles can couple with the internal modes over large distances. The experimental BSW resonances are a bit wider than the simulated BSW modes. This effect is possibly due to convolution with the angular aperture of the fiber bundle used in collection. Other reasons for the wider experimental spectra could be higher absorption losses due to the fluorophores distributed within the PVA film. The angle-dependent emission spectra evolution with PVA thicknesses from 0 to 60 nm were simulated and displayed for BWCE-dominant angular range 1 in Figure S9A and IMCE-dominant angular range 2 in Figure S9B. As PVA thickness increases, BWCE emission maxima displayed more than a 7-fold increase in the intensity, a shift to longer wavelengths and to slightly larger angles. The IMCE emission maxima, on the other hand, only increased by 2-fold in intensity with no other impact due to the PVA layer growth. The different sensitivity to thickness is due to the surface localization of the BSW as compared with the spatial distribution of the IM mode inside 1DPC (Figure 7).

It is of interest to understand the effect of the distance of the dipole from the surface on coupling with the modes existing in the 1DPC. Simulations were performed for an unpolarized dipole considering an incoherent sum from all three orthogonal orientations at distances of 5, 200 and

500 nm (Figure 12). The PVA thickness remained at 30 nm, so the more distant dipoles were in air. This was necessary because the BSW does not exist for the present structure with thicker polymer layer [54,55]. At a short 5 nm distance from the surface, in 30 nm PVA, the coupled emission was dominated by S-polarized coupling to the BSW mode. When the dipole is 200 or 500 nm from the surface there is no BSW-coupled emission, and the coupled emission is almost completely P-polarized. Additionally, the S-polarized emission spectra depends on distance, but the P-polarized emission spectra display smaller shifts and are less systematic (Figure 13). These results suggest that polarization measurements of coupled emission can be used for selective detection for surface-bound or bulk phase fluorophores.

A movie of raw intensity field evolving with increasing wavelength was provided in the supplementary material Figure S10 for $\vec{Y}$-oriented dipole that contributes to the S-polarized radiation, Figure S11 and S12 for the $\vec{X}$- and $\vec{Z}$-oriented dipoles, respectivey, that both contribute to P-polarized radiation. Both S- and P-polarized fields exhibited emission angular shifts with wavelength changing. However, the P-polarized field showed inherently less sensitive angular response with wavelength sweeping. Even after the spectral weighting in Figure S13, the P-polarized field spectral dispersions were still much weaker than S-polarized field. This agrees well with Figure 7 with only slight drops in P-polarized reflectivity above the critical angle.

Conclusions

In conclusion, the emission spectral properties of Ru probe in contact with a one-dimensional photonic crystal (1DPC) structure have been investigated. The wide unstructured emission from Ru probe can be shaped into two emission band spectra (BWCE and IMCE) that were highly dependent on the observation angle. This occurred for the S-polarized emission spectra, while the P-polarized emission spectra displayed smaller spectral shifts and/or non-systematic spectral changes. The BWCE resulted from the surface localized BSW-coupling which was limited for wavelengths smaller than 640 nm in both experiments and simulations, while the IM mode coupling emission, IMCE, was covering a wider spectral range, towards longer wavelengths in our case. This was confirmed by calculating the angularly and spectrally-resolved reflectivity map (dispersion diagram) that indicates the optical modes supported by the 1DPC structure. The experimental results were in good agreement with FDTD simulated emission from a near-field dipole located on top of the 1DPC. Measurements and simulations at larger wavelengths, where the BSW was not supported, showed that internal modes can also be exploited as detection channels of surface-bound fluorophores. Coupling efficiencies can be remarkably enhanced by choosing probes with broader wavelength emission spectrum.

CRediT authorship contribution statement

R. Badugu: Conceptualization, Methodology, Investigation, Writing. S. Blair: Simulations, Resources, Writing – review & editing, Visualization. E. Descrovi: Software, Simulations, Resources, Writing – review & editing, Visualization. J.R. Lakowicz: Validation, Resources, Formal analysis, Writing – original draft – review & editing, Supervision.

Declaration of competing interest

The authors declare that they have no known competing financial interests or personal relationships that could have appeared to influence the work reported in this paper.

Acknowledgments: The authors thank Dr. Jieying Mao for her substantial contributions to the near-field simulations. Dr. Steve Blair acknowledges the support and resources of the Center for High Performance Computing at the University of Utah, and support from the ECCS Division of NSF (award 1810096). Ramachandram Badugu and Joseph R. Lakowicz thank the NIH, National Institute of General Medical Sciences for support under R35 GM14414.

References

1. Weber, G. (1952). Polarization of the fluorescence of macromolecules, I: theory and experimental method, *Biochem. J.*, 51:145-155.
2. Millar, D. P. (1996). Time-resolved fluorescence spectroscopy, *Current Opinion in Structural Biology*, 6:637-642.
3. Johnson, I., and Spence, M. T. Z. (Eds). (2010). *The Molecular Probes Handbook. 11th Ed.*, Life Technologies Corp.
4. Mason, W. T. (Ed.) (1999). *Fluorescent and Luminescent Probes for Biological Activity*, 2nd Ed. Life Science Resources, UK 647 pp.
5. Vashist, S. K., and Luong, J. H. T. (Eds). (2018). *Handbook of Immunoassay Technologies: Approaches, Performances, and Applications,* 1st Ed. Academic Press, 496 pp.
6. Pawley, J. (Ed.) (2006). *Handbook of Biological Confocal Microscopy,* 3rd Ed. Springer, New York, 985 pp.
7. Mondal, P. P. And Diaspro, A. (Eds). (2015). *Fundamentals of Fluorescence Microscopy*, Springer, New York, 218 pp.

8. Lakowicz, J. R. (2001). Radiative decay engineering: Biophysical and biomedical applications, *Anal. Biochem.*, 298:1-24.
9. Lakowicz, J. R., Shen, Y., D'Auria, S., Malicka, J., Fang, J., Gryczynski, Z., and Gryczynski, I. (2002). Radiative decay engineering 2. Effects of silver island films on fluorescence intensity, lifetimes, and resonance energy transfer, *Anal. Biochem.*, 301:261-277.
10. Raether, H. (1988). *Surface Plasmons on Smooth and Rough Surfaces and on Gratings*, Springer-Verlag, New York, 136 pp.
11. Brongersma, M. L., and Kik, P. G. (Eds.) (2008). *Surface Plasmon Nanophotonics*, Springer, New York, 268 pp.
12. Lakowicz, J. R. (2005). Radiative decay engineering 5: metal-enhanced fluorescence and plasmon emission, *Anal. Biochem.*, 337:171-194.
13. Deng, W., and Goldys, E. M. (2023). Plasmonic approach to enhanced fluorescence for applications in biotechnology and the life sciences, *Langmuir*, 28:10152-10163.
14. Jeong, Y. Kook, Y-M., Lee, K., Koh, W-G. (2018). Metal enhanced fluorescence (MEF) for biosensors: General approaches and a review of recent developments, *Biosensors and Bioelectron.*, 111:102-116.
15. Bauch, M., Toma, K., Toma, M., Zhang, Q., and Dostalek, J. (2014). Plasmon-enhanced fluorescence biosensors: A review, *Plasmonics*, 9:781-799.
16. Luan, J., Morrissey, J. J., Wang, Z., Derami, H. G., Liu, K-K., Cao, S., Jiang, Q., Wang, C., Kharasch, E. D., Nalk, R. R., and Singamaneni, S. (2018). Add-on plasmonic patch as a universal fluorescence enhancer, *Light: Sci Appl.*, 7:29-1/13.

17. Lakowicz, J. R. (2004). Radiative decay engineering 3. Surface plasmon-coupled directional emission, *Anal. Biochem.,* 324:153-169.
18. Gryczynski, I., Malicka, J., Gryczynski, Z., and Lakowicz, J. R. (2004). Radiative decay engineering 4. Experimental studies of surface plasmon-coupled directional emission, *Anal. Biochem.,* 324:170-182.
19. Jiang, Y., Wang, H-Y., Wang, H., Gao, B-R., Hao, Y-w., Jin, Y., Chen, Q-D., and Sun, H-B (2011). Surface plasmon enhanced fluorescence of dye molecules on metal grating films, *J. Phys. Chem. C.,* 115:13636-12642.
20. Aouani, H., Mahboub, O., Bonod, N., Devaux, E., Popov, E., Rigneault, H., Ebbesen, T. W., and Wenger, J. (2011). Bright unidirectional fluorescence emission of molecules in a nanoaperture with plasmonic corrugations, *Nano Letts.*, 11:637-644.
21. Joannopoulos, J. D., Johnson, S. G., Winn, J. N., and Meade, R. D. (Eds.) (2008). *Photonic Crystals. Molding the Flow of Light*., Princeton University Press, 286 pp.
22. Saleh, B. E. A., and Teich, M. C. (Eds.) (2007). *Fundamentals of Photonics, 2nd Ed*., John Wiley, 1177 pages.
23. Novotny, L., and Hecht, B. (Eds.) (2006). *Principles of Nano-Optics*., Cambridge University Press, 539 pp.
24. Gaponenko, S. V. (2010). *Introduction to Nanophotonics*., Cambridge University Press, 465 pp.
25. Koenderink, A. F., Kafesaki, M., Soukoulis, C. M., and Sandoghdar, V. (2005). Spontaneous emission in the near field of two-dimensional photonic crystals, *Optics Letts.*, 30:3210-3212.

26. Zhang, W., Ganesh, N., Mathias, P. C., and Cunningham, B. T. (2008). Enhanced fluorescence on a photonic crystal surface incorporating nanorod structures, *Small.*, 12:2199-2203.
27. Estrada, L. C., Martinez, O. E., Brunstein, M., Bouchoule, S., Le-Gratiet, L., Talneau, A., Sagnes, I., Monnier, P., Levenson, J. A., and Yacomotti, A. M. (2010). Small volume excitation and enhancement of dye fluorescence on a 2D photonic crystal surface, *Opt. Express*, 18:3693-3699.
28. Ganesh, N., Zhang, W., Mathias, P. C., Chow, E., Soares, J.A.N.T., Malyarchuk, V., Smith, A. D., and Cunningham, B. T. (2007). Enhanced fluorescence emission from quantum dots on a photonic crystal, *Nature Nanotech.,* 2:515-520.
29. Kubo, S., Fujishima, A., Sato, O., and Segawa, H. (2009). Anisotropic accelerated emission of the chromophores in photonic crystals consisting of a polystyrene opal structure, *J. Phys. Chem. C.,* 113:11704-11711.
30. Bechger, L., Lodahl, P., and Vos, W. L. (2005). Directional fluorescence spectra of laser dye in opal and inverse photonic crystals, *J. Phys. Chem. B.,* 109:9980-9988.
31. Zhou, Z-K., Lei, D. Y., Liu, J., Liu, X., Xue, J., Zhu, Q., Chen, H., Liu, T., Li, Y., Zhang, H. and Wang, X. (2014). Shaping the emission spectral profile of quantum dots with periodic dielectric and metallic nanostructures, *Adv. Opt. Mat.,* 2:56-64.
32. Lee, R-K., and Lai, Y. (2004). Fluorescence squeezing spectra near a photonic bandgap, *J. Opt B., Quan Semi Opt.*, 6:S715-S721.
33. Gaponenko, S. V., Bogomolov, V. N. Petrov, e. P., Kapitonov, A. M., Eychmueller, A. E., Rogach, A. L., Kalosha, I. I., Gindele, F., and Woggon, U. (2000). Spontaneous emission

of organic molecules and semiconductor nanocrystals in a photonic crystal, *J. Luminescence*, 87-89:152-156.

34. Liscidini, M., Galli, M., Shi, M., Dacarro, G., Patrini, M., Bajoni, D. and Sipe, J. E. (2009). Strong modification of light emission from a dye monolayer via Bloch surface waves, *Opt. Letts.*, 34:2318-2320.
35. Jiang, P., Bertone, J. F., Hwang, K. S., and Colvin, V. L. (1999). Single-crystal colloidal multilayers of controlled thickness, *Chem. Mater.*, 11:2132-2140.
36. Park, M., Harrison, C., Chalkin, P. M., Register, R. A., and Adamson, D. H. (1997). Block copolymer lithography: Periodic arrays of 10^{11} holes in 1 square centimeter, *Science*, 276:1401-1404.
37. Cunin, F., Schmeadake, T. A., Link, J. R., Li, Y. Y., Koh, J., Bhatia, S. N., and Salor, M. J. (2002). Biomolecular screening with encoded porous-silicon photonic crystals, *Nature Materials*, 1:38-41.
38. Zhang, J-T., Smith, N., and Asher, S. A. (2012). Two-dimensional photonic crystal surfactant detection, *Anal. Chem.*, 84:6416-6420.
39. Zhang, J. T., Cai, Z., Kwak, D. H., Liu, X., and Asher, S. A. (2014). Two-dimensional photonic crystal sensors for visual detection of lectin concanavalin A., *Anal. Chem.*, 85:9036-9041.
40. Ballarini, M., Frascella, F., Michelotti, F., Digregorio, G., Rivolo, P., Paeder, V., Musi, V., Giorgis, F., and Descrovi, E. (2011). Bloch surface waves-controlled emission of organic dyes grafted on a one-dimensional photonic crystal, *Appl. Phys. Letts.*, 99:043302.

41. Zhang, D., Badugu, R., Chen, Y., Yu, S., Yao, P., Wang, P., Ming, H., and Lakowicz, J. R. (2014). Back focal plane imaging of directional emission from dye coupled to one-dimensional photonic crystals, *Nanotech.*, 25:145202-1/10.

42. Badugu, R., Nowaczyk, N., Descrovi, E., and Lakowicz, J. R. (2013). Radiative decay engineering 6: Fluorescence on one-dimensional photonic crystals, *Anal. Biochem.*, 442:83-96.

43. Kang, J. S., Piszczek, G., and Lakowicz, J. R. (2002). High-molecular weight protein hydrodynamics studied with a long-lifetime metal-ligand complex, *Biochim. Biophys. Acta*, 1597:221-228.

44. Gryczynski, I., Malicka, J., Nowaczyk, K., Gryczynski, Z., and Lakowicz, J. R. (2004). Effects of sample thickness on the optical properties of surface plasmon-coupled emission, *J. Phys. Chem. B.*, 108:12073-12083.

45. TFCalc, Light Tec GMBH, Munich, Germany.

46. Lumerical Solutions, Inc., Vancouver, BC, Canada.

47. Descrovi, E., Sfez, T., Dominici, L., Nakagawa, W., Michelotti, F., Giorgis, F., Herzig, H.-P. (2008). Near-field imaging of Bloch surface waves on silicon nitride one-dimensional photonic crystals, *Optics Exp.*, 16:5453-5464.

48. Robertson, W. M., and May, M. S. (1999). Surface electromagnetic wave excitation on one-dimensional photonic band-gap arrays, *Appl. Phys. Letts.*, 74:1800-1802.

49. Lakowicz, J. R. (2006). *Principles of Fluorescence Spectroscopy*, 3rd edition, Springer, 954 pp.

50. Hecht, E. (2002). *Optics*, 4th ed. Adelphi Univ, 698 pp.

51. Badugu, R., Mao, J., Blair, S., Zhang, D., Descrovi, E., Angelini, A., Huo, Y., and Lakowicz, J. R. (2016). Bloch surface wave-coupled emission at ultraviolet wavelengths, *J. Phys. Chem. C.*, 120:28727–28734.
52. Perani, T., Liscidini, M. (2020). Long-range Bloch surface waves in photonic crystal ridges, *Opt. Lett.* 45: 6534-6537
53. Vosoughi, B., Descharmes, N., Barbey, R., Osowiecki, G. D., Wittwer, V. J., Razskazovskaya, O., Südmeyer, T., Herzig, H.-P. (2022). Centimeter-Scale Propagation of Optical Surface Waves at Visible Wavelengths. *Adv. Optical Mater.*, 10, 2102854.
54. Sfez, T., Descrovi, E., Dominici, L., Nakagawa, W., Michelotti, F., Giorgis, F., and Herzig, H.-P. (2008). Near-field analysis of surface electromagnetic waves in the bandgap region of a polymeric grating written on a one-dimensional photonic crystal, *Appl. Phys. Letts.*, 93: 061108.
55. Meade, R. D., Brommer, K. D., Rappe, A. M., and Joannopoulos, J. D. (1991). Electromagnetic Bloch waves at the surface of a photonic crystal, *Phys. Rev. B.*, 44:10961-10964.

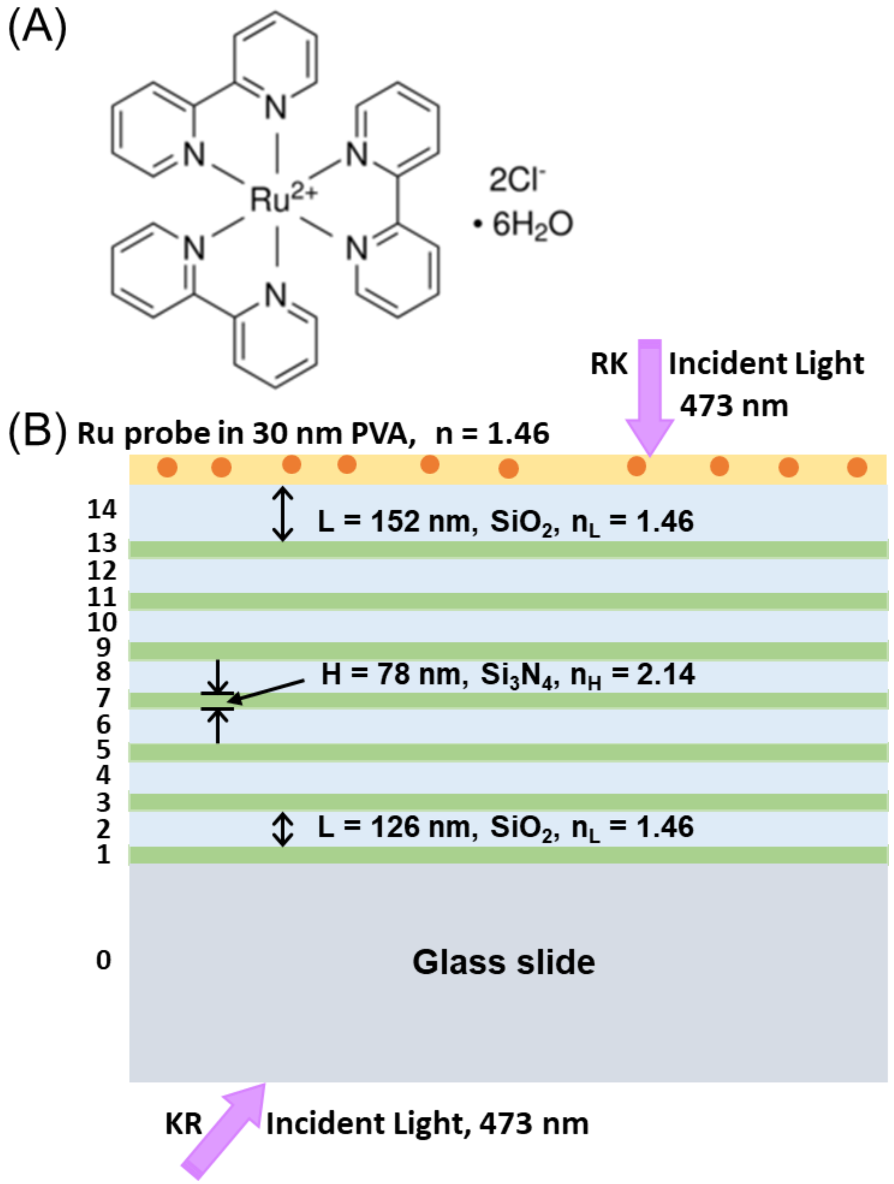

Figure 1. (A), molecular structure of the Ru probe [Ru(bpy)$_3$Cl$_2$] used in the present study. (B), schematic of the SiO$_2$ - Si$_3$N$_4$ multilayers in the 1DPC used, and the optical constants. Also shown is the final PVA layer which contains Ru probe.

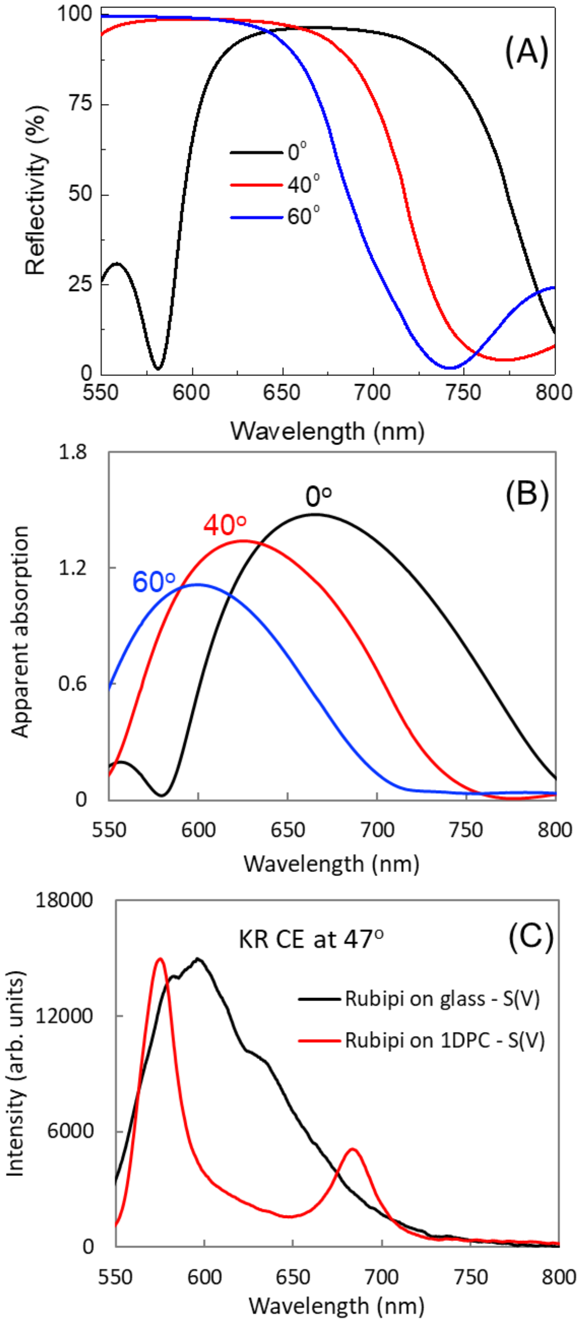

Figure 2. (A), Calculated unpolarized reflectivity of the 1DPC shown in Figure 1B at various angles of incidence. (B), Unpolarized apparent absorption spectra with incident angle increasing from 0° to 60°. (C), S-polarized emission spectra of Ru probe observed at 47° from glass and 1DPC. KR excitation at 48° using 470 nm light.

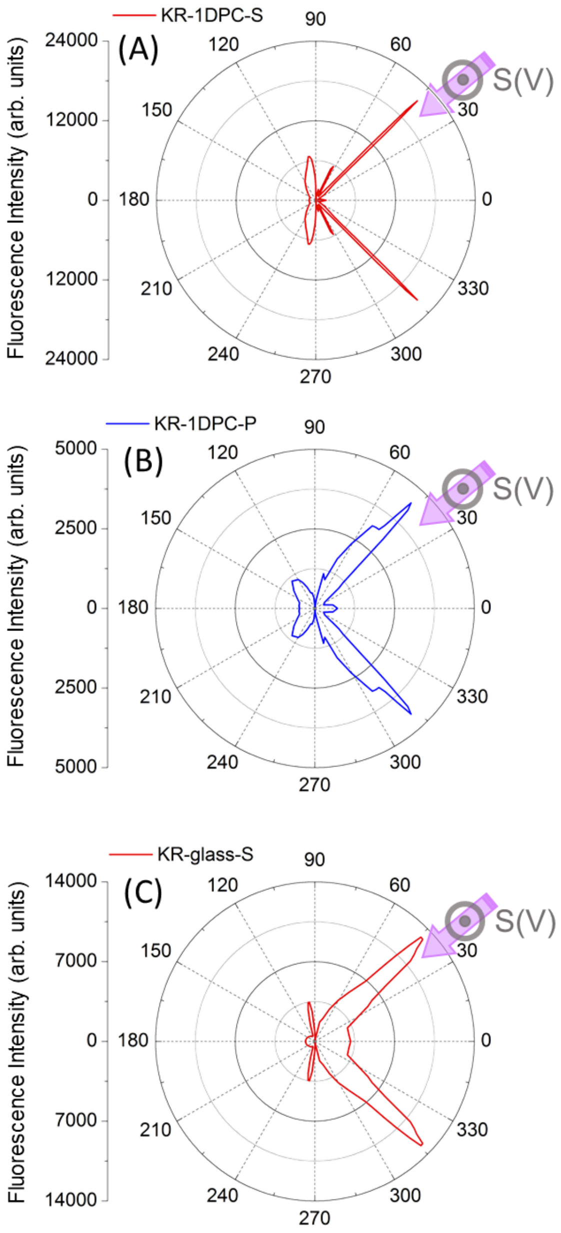

Figure 3. The angular distribution of S- and P- polarized 600 nm emission from Ru probe on 1DPC (A, B, respectively) and angular distribution of Ru probe S-polarized emission on glass (C) with 473 nm KR excitation at 48° using V-polarized incident light.

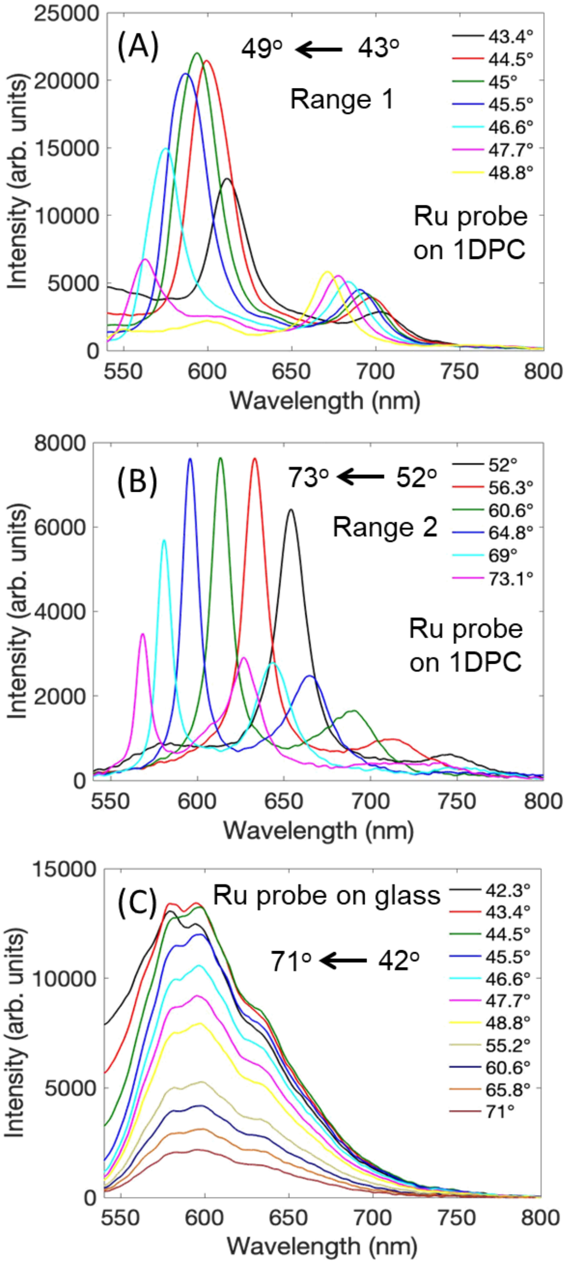

Figure 4. (A), Effect of observation angle in Range 1 (43 – 49°) and (B) in Range 2 (52 – 73°) on the S-polarized coupled emission spectra of Ru probe on 1DPC and (C) that of on glass using V-polarized 473 nm light and KR excitation at 48°.

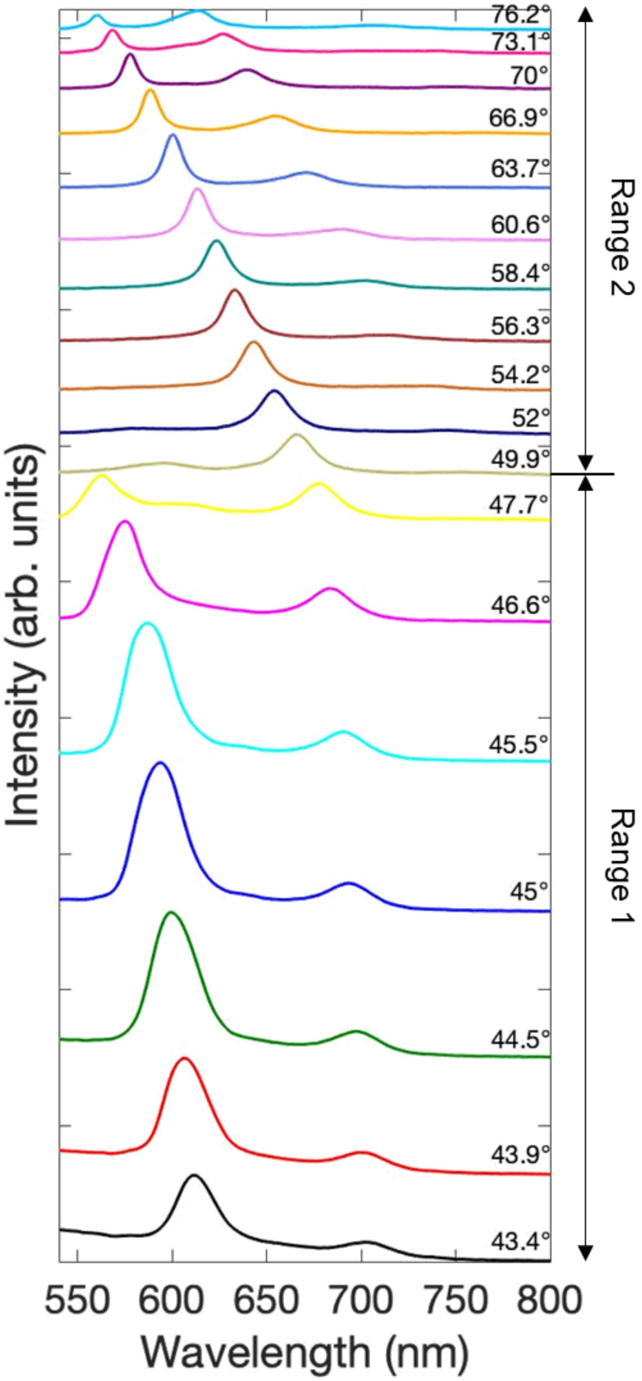

Figure 5. Effect of observation angle on the S-polarized coupled emission spectra of Ru probe on the 1DPC using KR, 473 nm light excitation at 48º. Y-scale is adjusted for clarity.

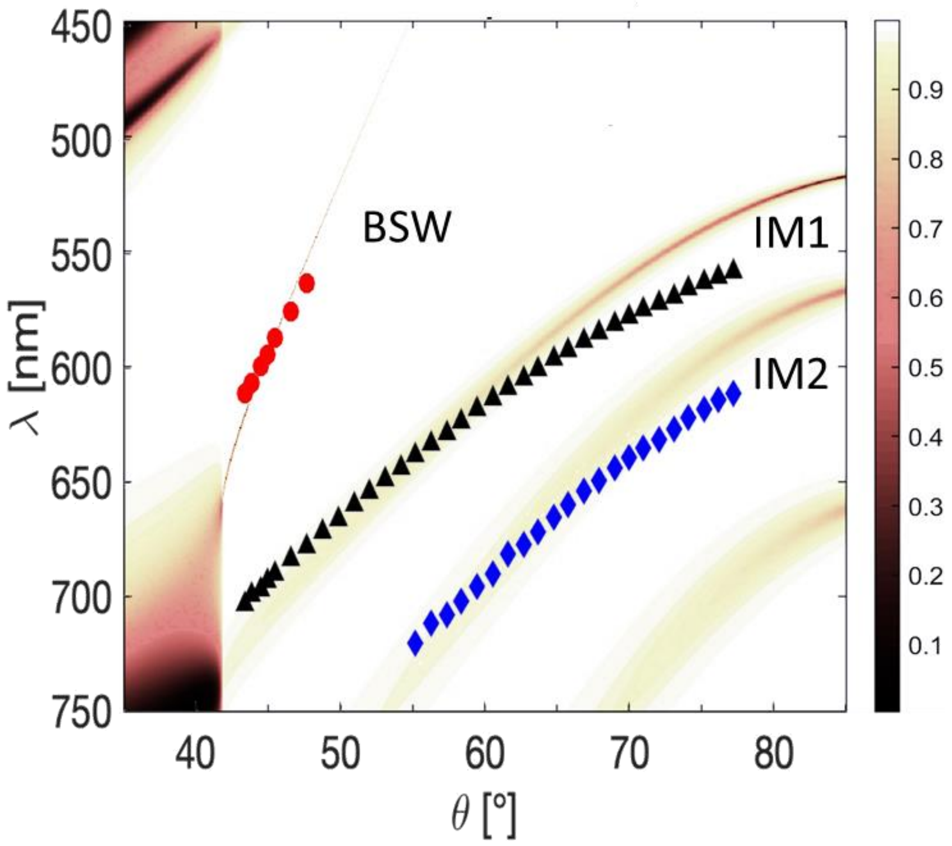

Figure 6. Dispersion diagram for the 1DPC shown in Figure 1B. The figure shows the reflectivity for a range of wavelengths and incidence angles. The circles, triangles, or diamonds represent the emission maxima for respective angles from Figures 5.

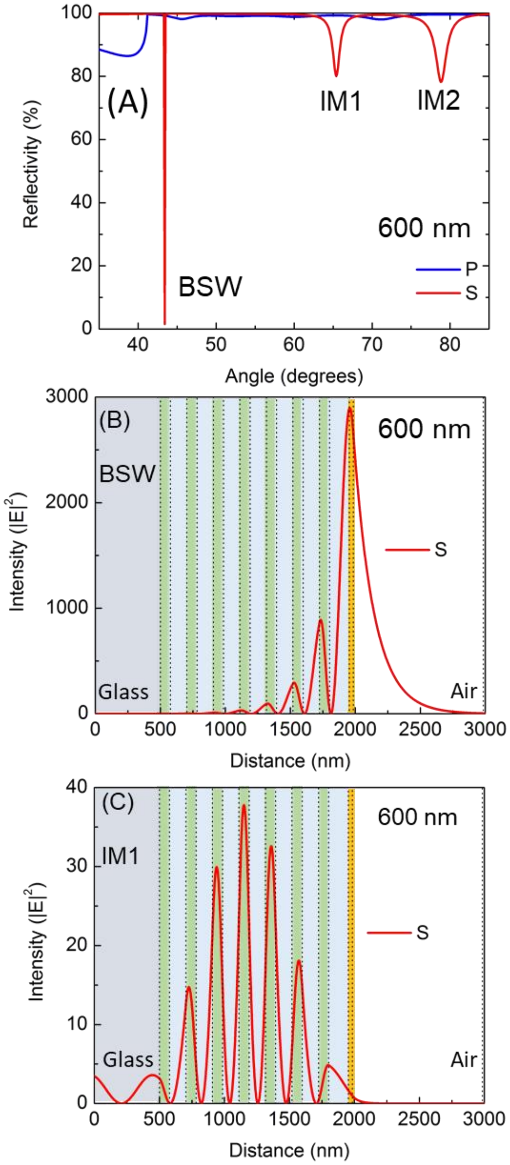

Figure 7. (A), 1DPC reflectivity and (B and C), electric field intensities (|E|^2) distribution for 600 nm incident light at the BSW resonance angle (43.4°) and IM1 angle (65.4°), respectively. Both S- and P- polarized reflectivities were shown in the angle dependent reflectivity (A), and only S-polarized field distributions for BSW and IM modes were presented in panels (B and C), respectively.

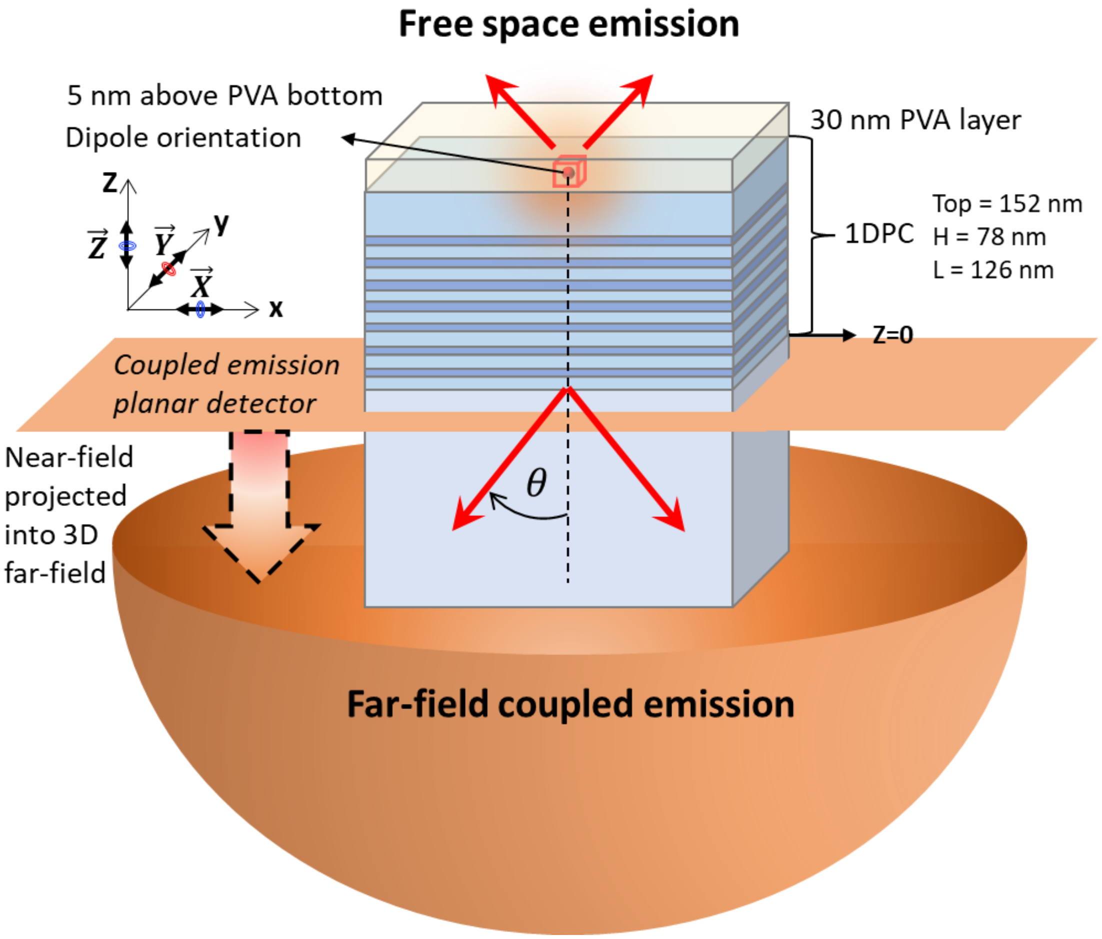

Figure 8. Schematic model of the 2D simulation in x-z plane. Single dipole simulations were calculated using $\vec{X}$, $\vec{Z}$, and $\vec{Y}$ orientations separately. Electric field intensity of a $\vec{Y}$-oriented dipole source has mostly a y-axis component that is analogous to S(V)-polarization in the experiments and is termed as $|E_Y|^2 = |E_s|^2$. The electric field intensities calculated with $\vec{X}$- and $\vec{Z}$-oriented dipole contribute to the analogous emission of P(H)-polarization in the experiments. The sum of their intensity results is referred as $|E_X|^2 + |E_Z|^2 = |E_p|^2$.

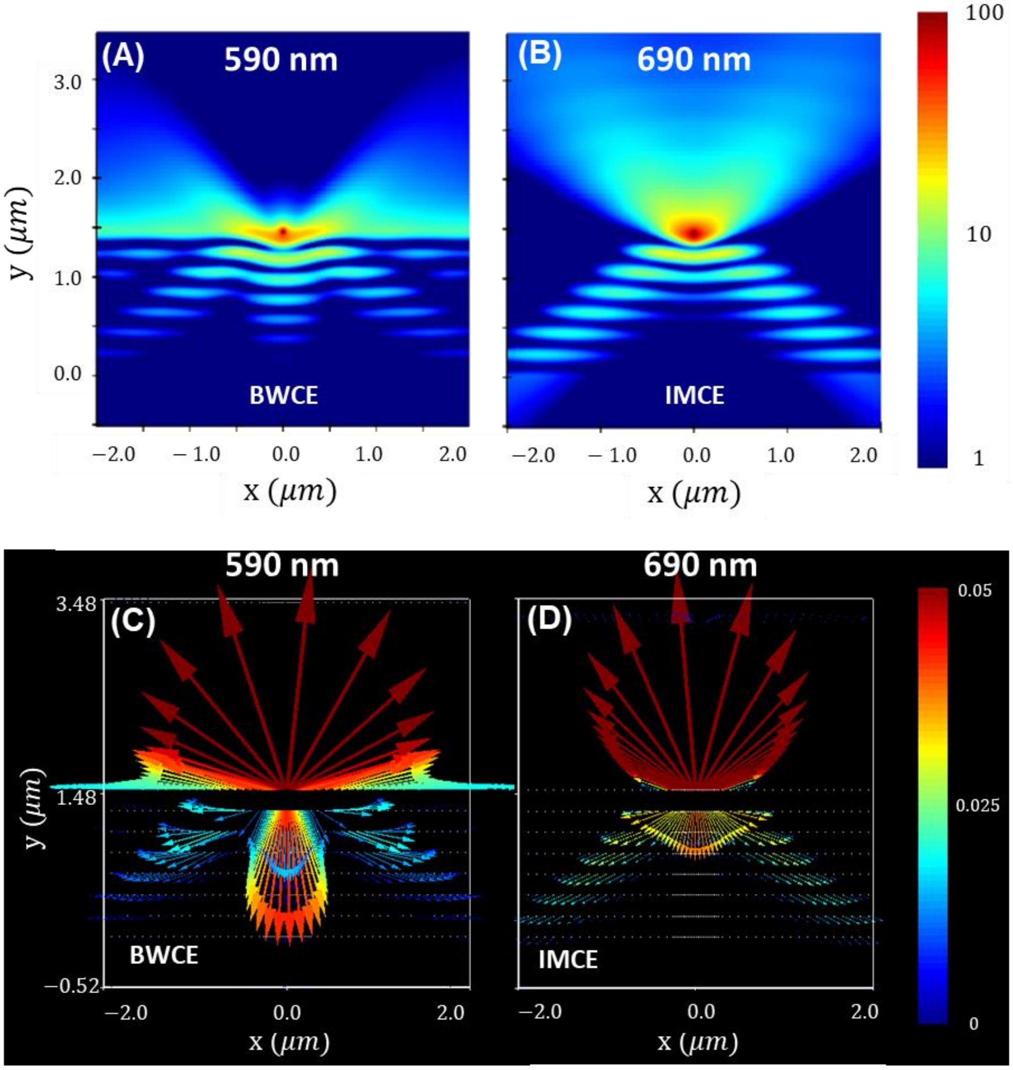

Figure 9. Electric field (A and B) and Poynting vector field distribution (C and D) in 1DPC and free space side using a $\vec{Y}$-oriented dipole source at selected resonances of 590 and 690 nm, respectively. The $|E_s|^2$ was plotted under a logarithmic scaled color bar on the right side (top). The Poynting vector at each data point was plotted under a linear scaled color bar on the right side (bottom). The single wavelength simulations were calculated using Lumerical FDTD solutions. BWCE dominated in 590 nm field, while IMCE dominated in 690 nm field.

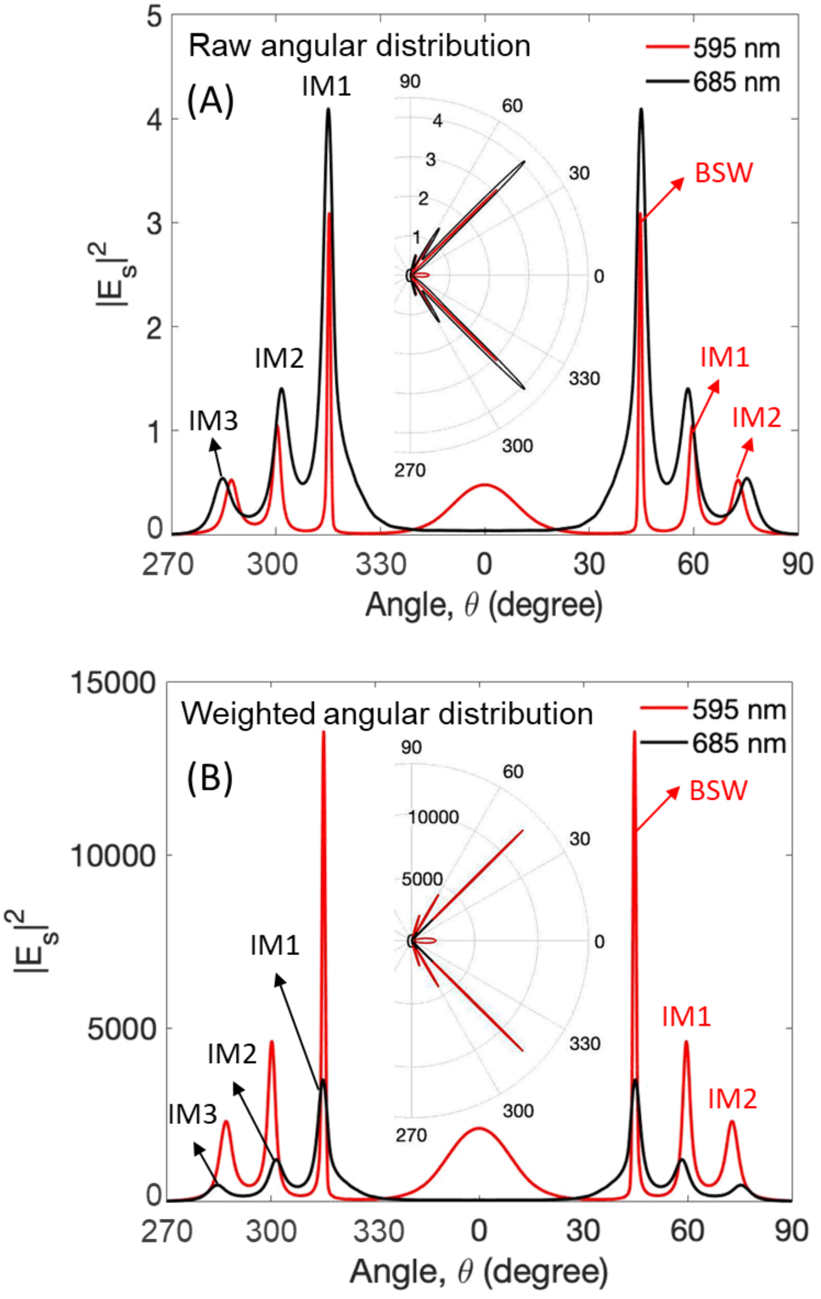

Figure 10. The far-field simulation results on 1DPC using a $\vec{Y}$-oriented single dipole source. (A), raw angular distribution of the far-field intensity at 595 and 685 nm. (B), weighted angular distribution of the far-field intensity at 595 and 685 nm. Inset polar plots are coupled emission angular distribution across all angles from 270 to 90°.

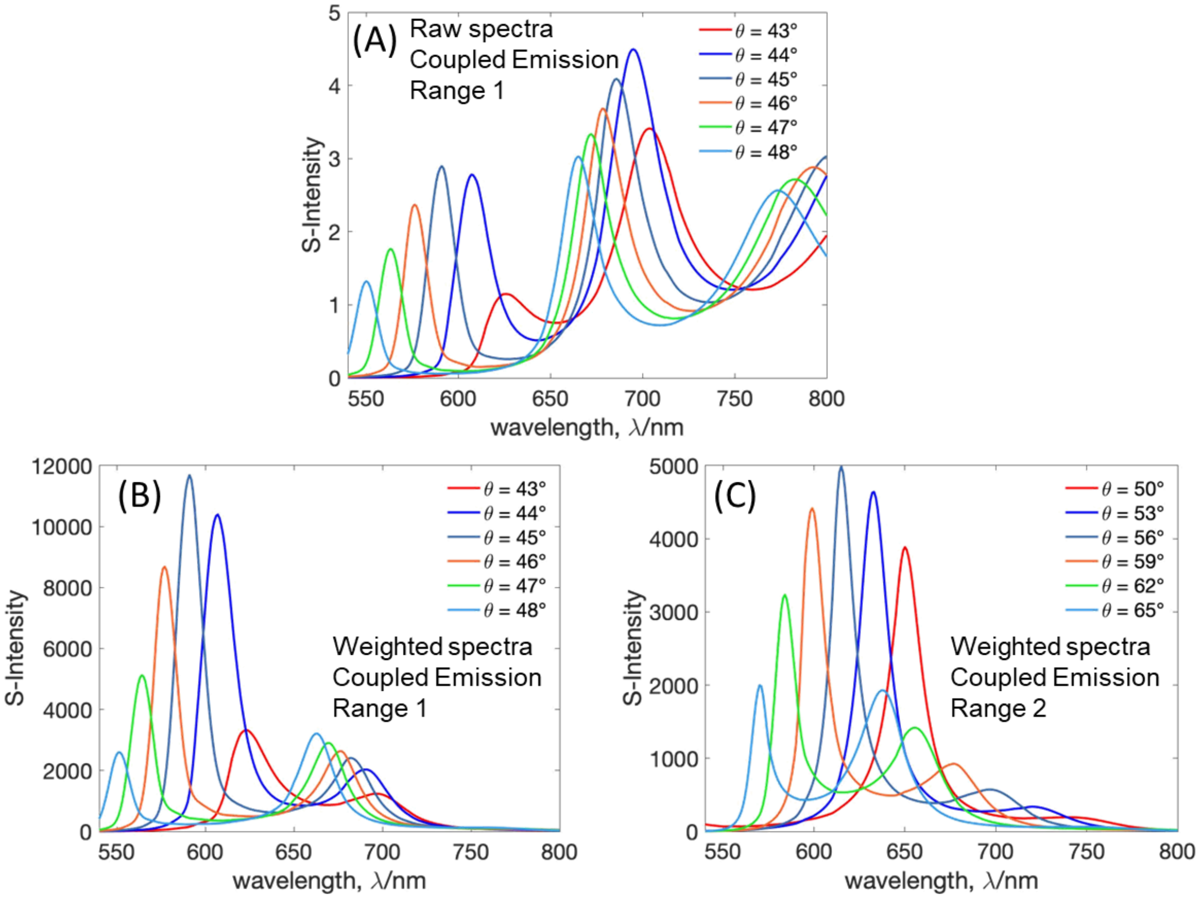

Figure 11. Effect of calculated angle on the emission spectra with a $\vec{Y}$-oriented dipole source. (A), the raw spectra of angular dependent coupled emission in Range 1 (43–48°). (B), weighted emission spectra in Range 1 (43–48°) and panel (C) shows weighted emission spectra for Range 2 (50–65°), which match with experimental data shown in Figures 4A and B, respectively.

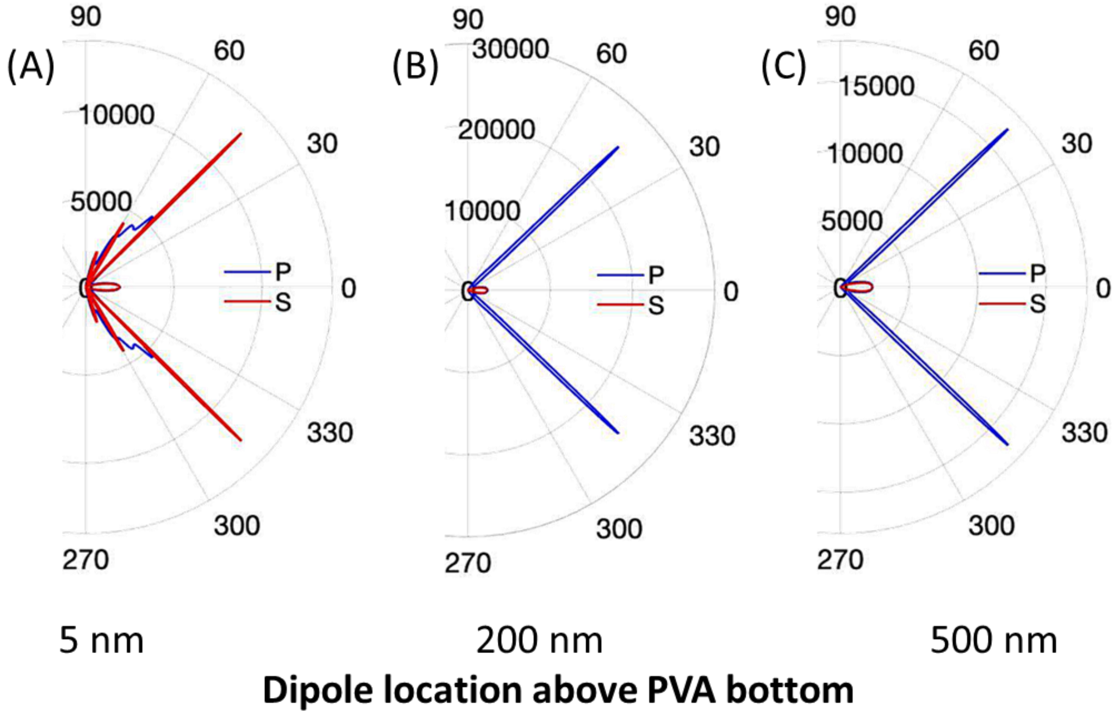

Figure 12. Effect of dipole-distance from the 1DPC on the emission intensity of a 600 nm dipole with $\vec{Y}$- (S) and $(\vec{X},\vec{Z})$- (P) orientation: angular distribution of simulated weighted coupled emission with dipole location set to be at (A) 5, (B) 200 (C) 500 nm above the bottom surface of the PVA layer. Dipole located at 5 nm has its emission maximum in S-polarized emission component at a slightly larger angle than the emission maxima in P-polarized emission component for dipole located at 200 and 500 nm.

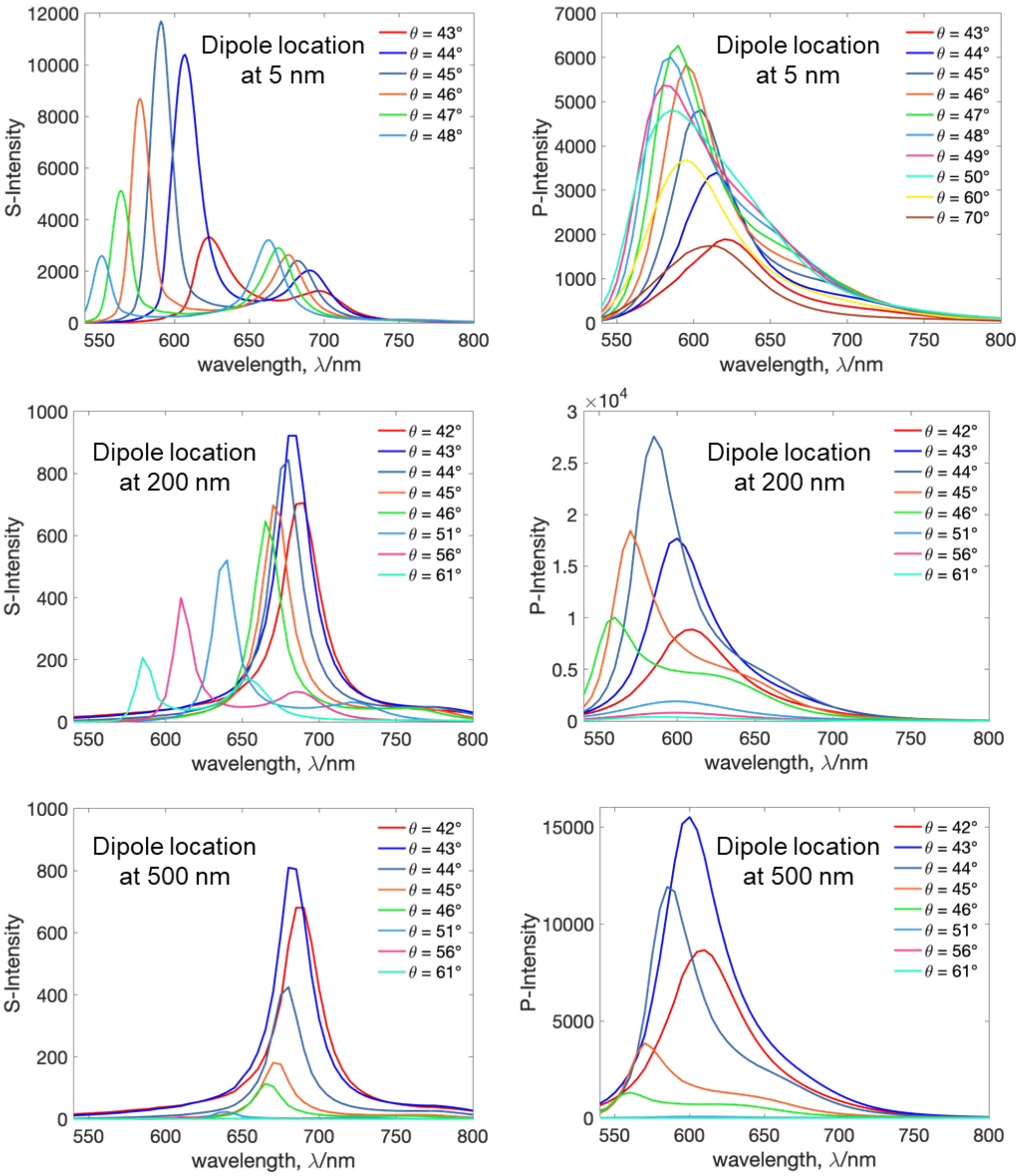

Figure 13. Effect of dipole-distance from the 1DPC on the angle-dependent simulated weighted S-polarized emission spectra from a $\vec{Y}$- oriented dipole (left) and on the simulated P-polarized emission spectra from a $(\vec{X}, \vec{Z})$- oriented dipole (right). From top panel to bottom panel, the dipole source is set to be at distances of 5, 200 and 500 nm above the bottom surface of PVA layer.

Supplementary Information

Fluorophore Interactions with the Surface Modes and Internal Modes of a Photonic Crystal

Ramachandram Badugu[1], *Steve Blair*[2], *Emiliano Descrovi*[3], *and Joseph R. Lakowicz*[1*]

[1]Center for Fluorescence Spectroscopy, Department of Biochemistry and Molecular Biology,
University of Maryland School of Medicine, Baltimore, MD 21201, United States.

[2]Department of Electrical and Computer Engineering, University of Utah, 50 South Central
Campus Drive, Room 2110, Salt Lake City, UT 84112, United States

[3]Department of Applied Science and Technology, Polytechnic University of Turin, corso Duca
degli Abruzzi 24, 10129 Turin, Italy

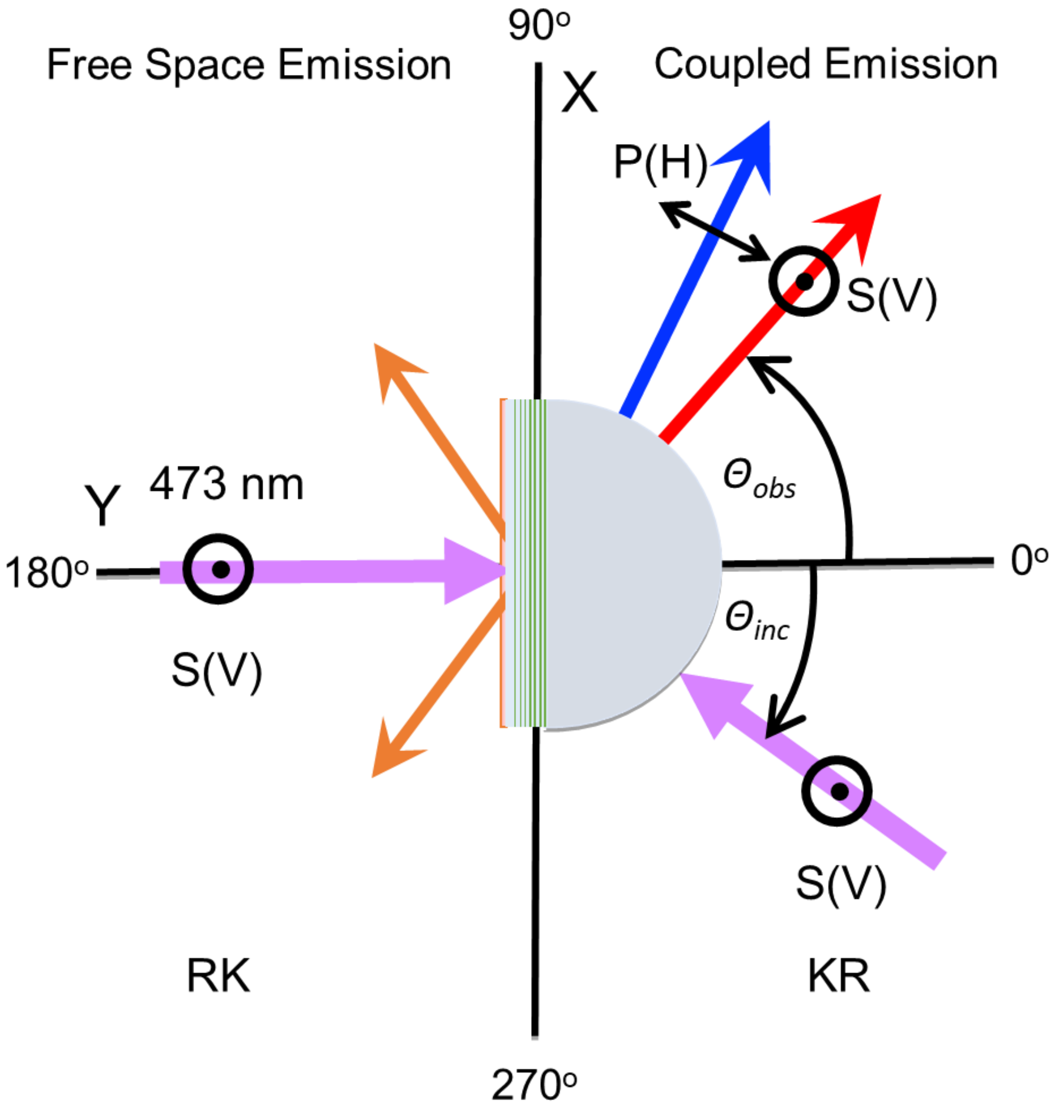

Figure S1. Top view (along the Z-axis) of the experimental geometry and polarization used with the 1DPC. The thin green lines represent the 1DPC high refractive index layers.

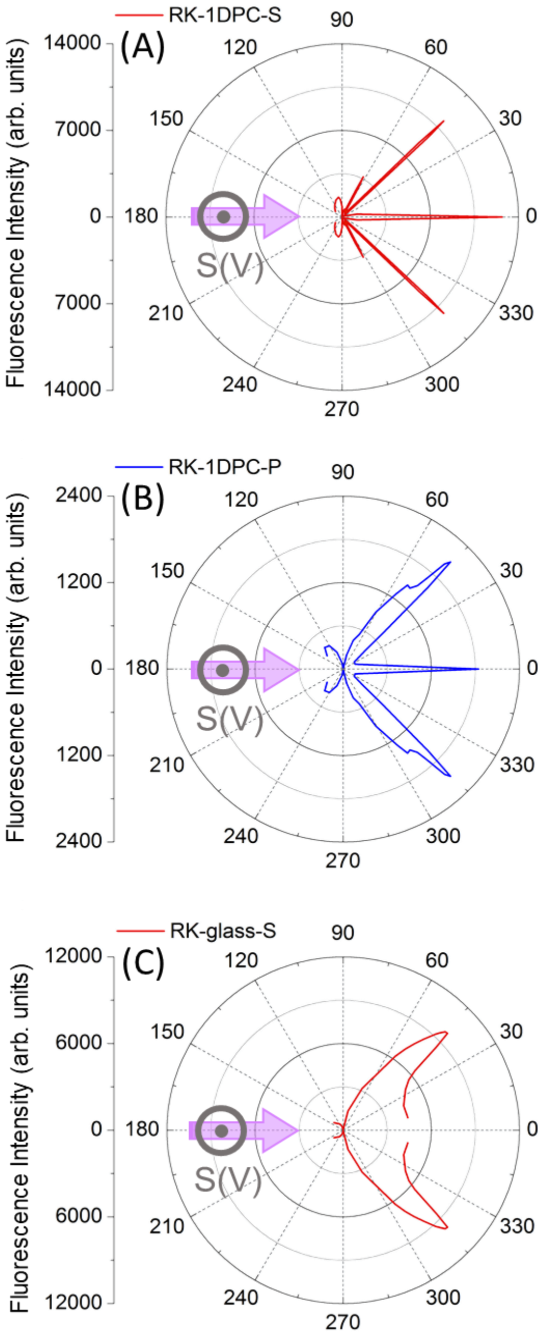

Figure S2. Angular distribution of S-and P-polarized emission from Ru Probe on 1DPC (A, B respectively) and Ru probe S-polarized emission from glass (C). RK illumination at 180^{o} using V-polarized 473 nm incident light.

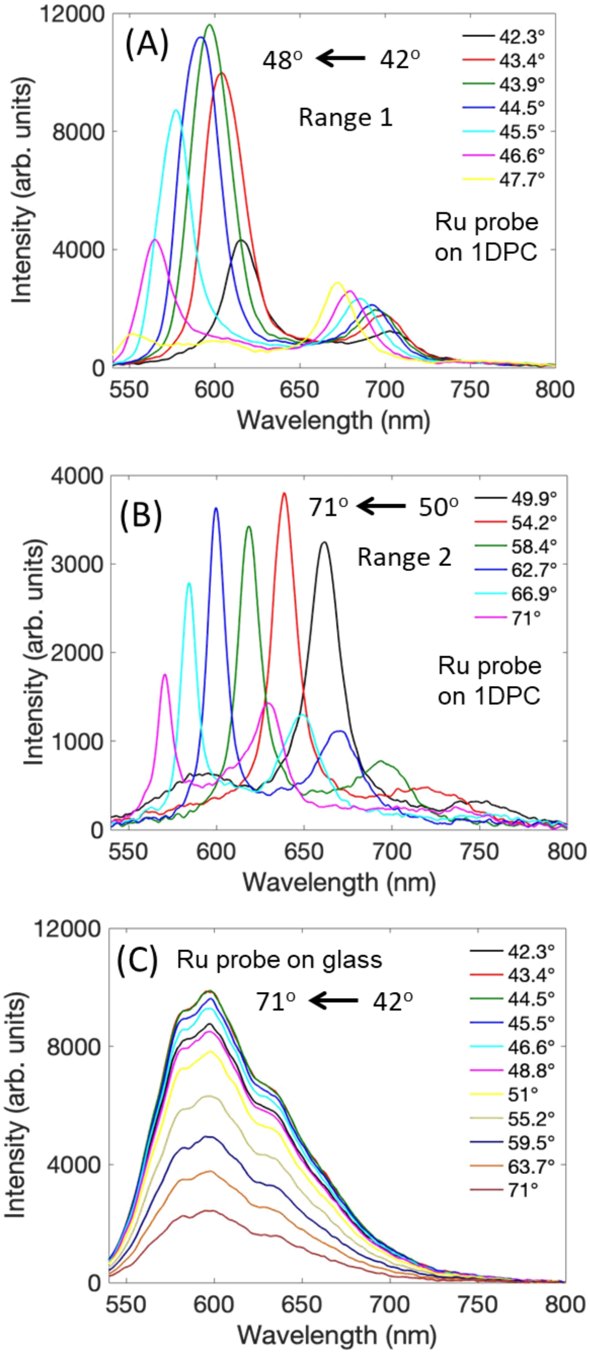

Figure S3. (A), Effect of observation angle in Range 1 (42 – 48°) and (B) in Range 2 (50 – 71°) on the S-polarized coupled emission spectra of Ru probe on 1DPC and that on glass (C). RK illumination at 180° using V-polarized 473 nm incident light.

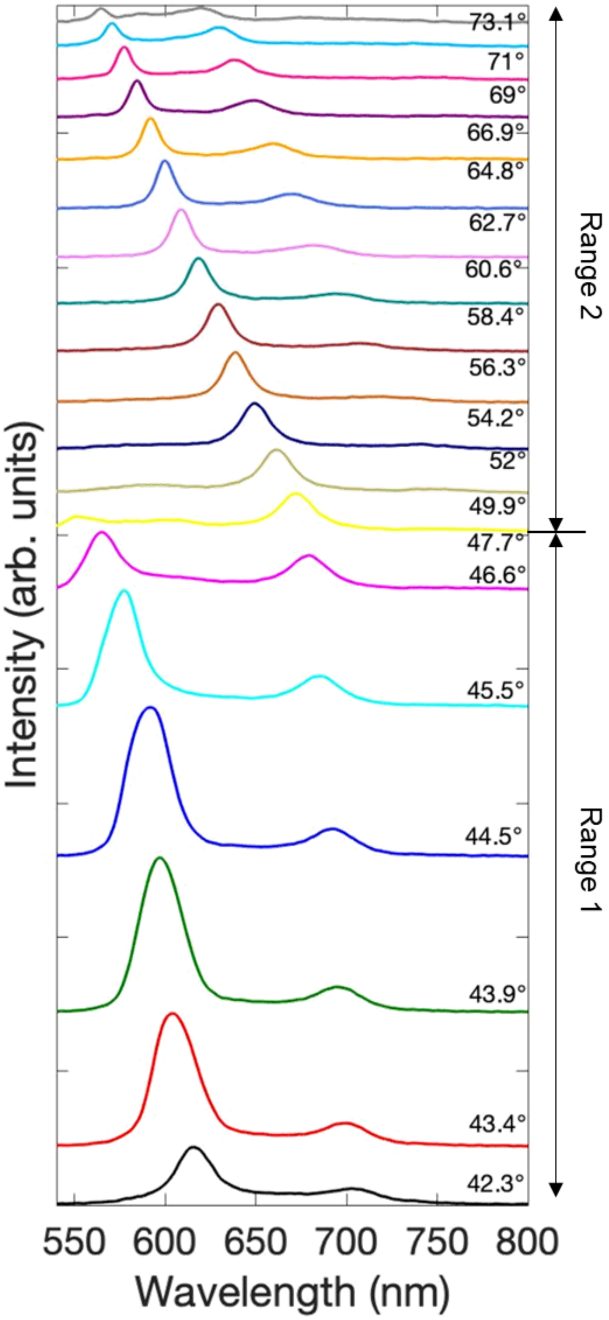

Figure S4. Effect of observation angle on the S-polarized coupled emission spectra of Ru probe from 42 to 73^{o} (both range 1 and range 2). RK illumination at 180^{o} using V-polarized 473 nm incident light. Y-scale is adjusted for clarity.

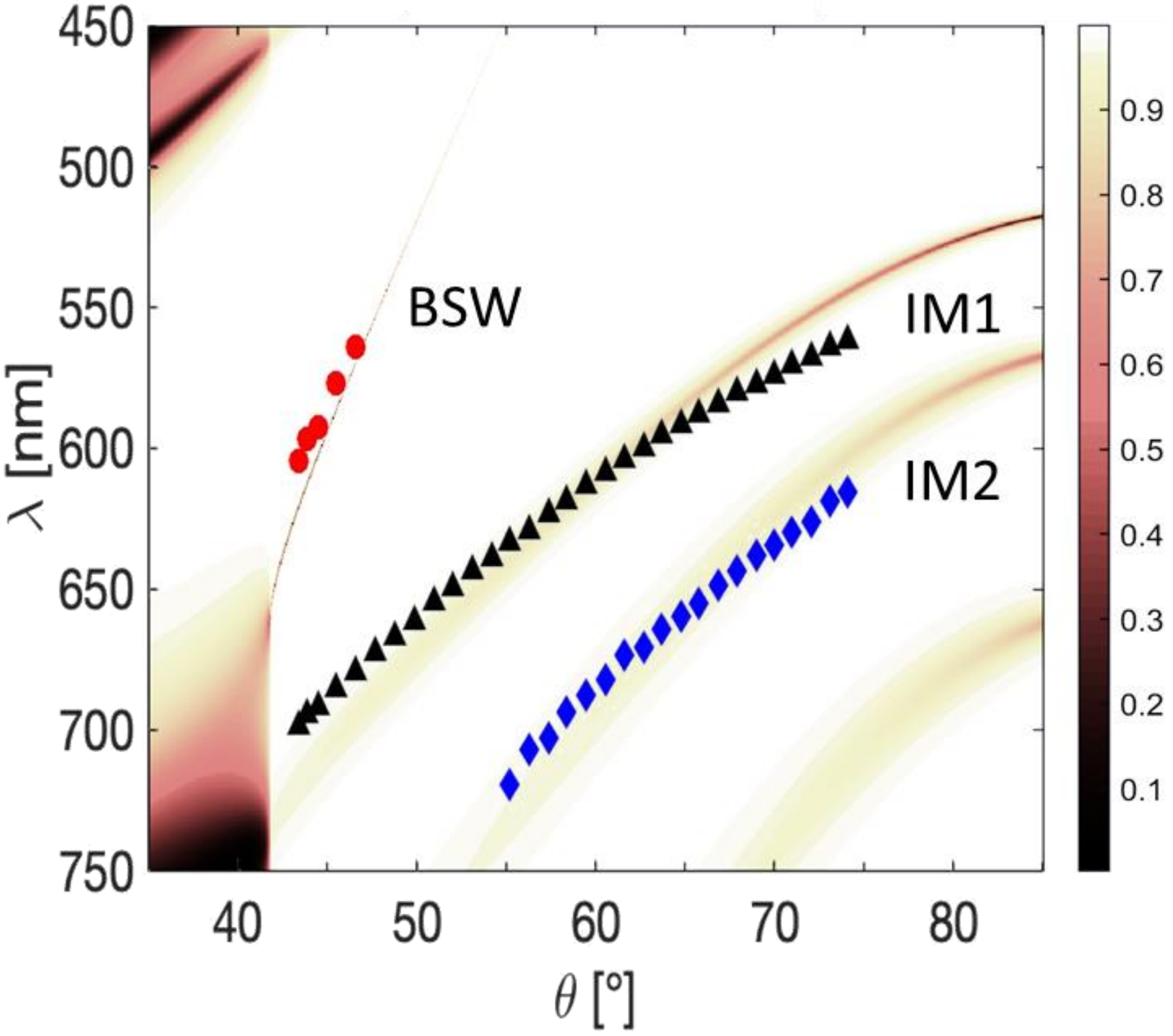

Figure S5. Dispersion diagram for the 1DPC shown in Figure 1B. The figure shows the reflectivity for a range of wavelengths and incidence angles. The circles, triangles, or diamonds represent the emission maxima for respective angles, from Figures S4.

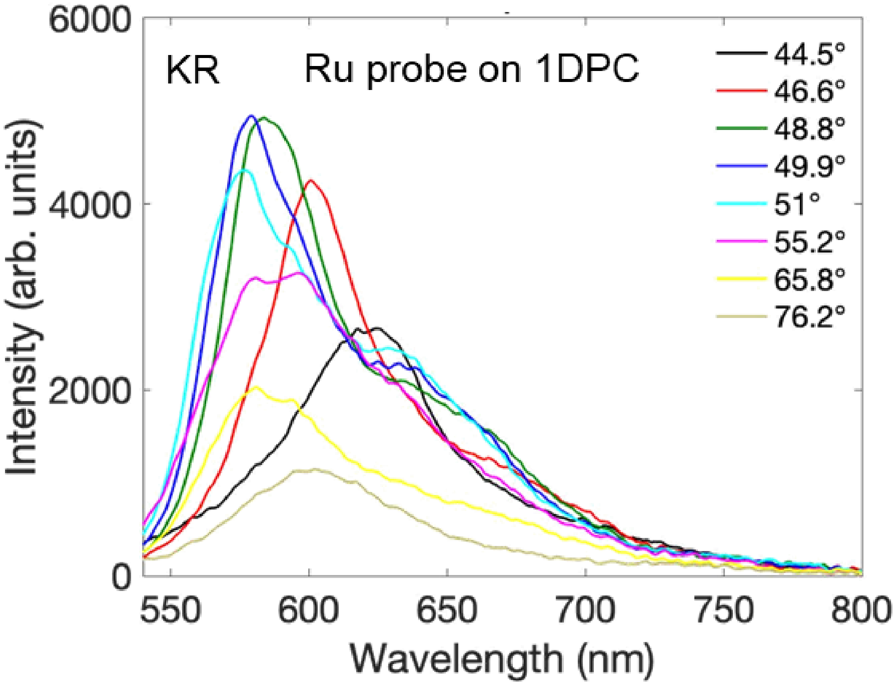

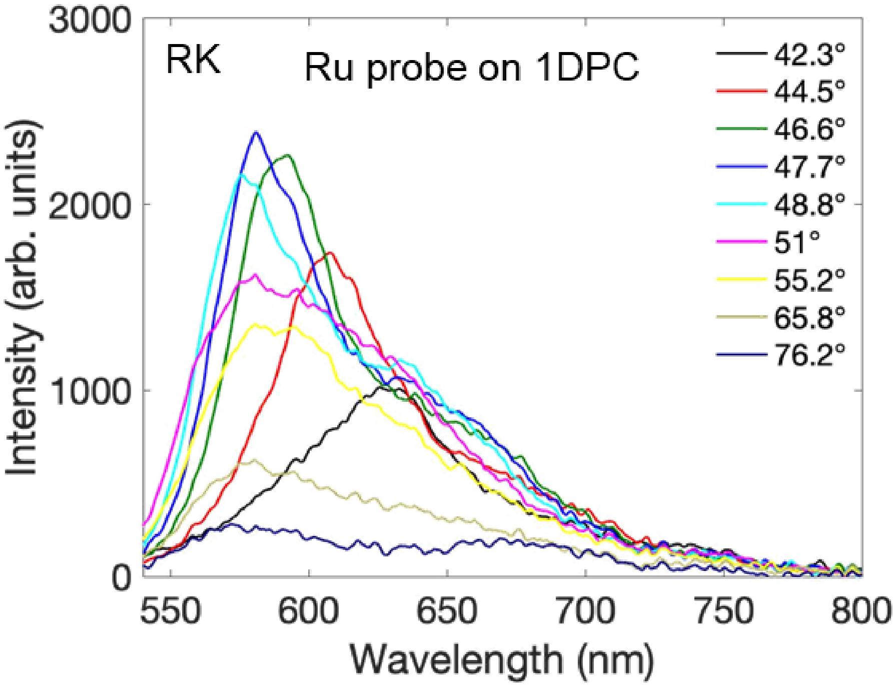

Figure S6. Angle-dependent P-polarized emission spectra of the Ru probe on 1DPC in Range 1 and Range 2 (44 – 76°). V-polarized 473 nm light, KR illumination at 48° (top) and RK illumination at 180° (bottom).

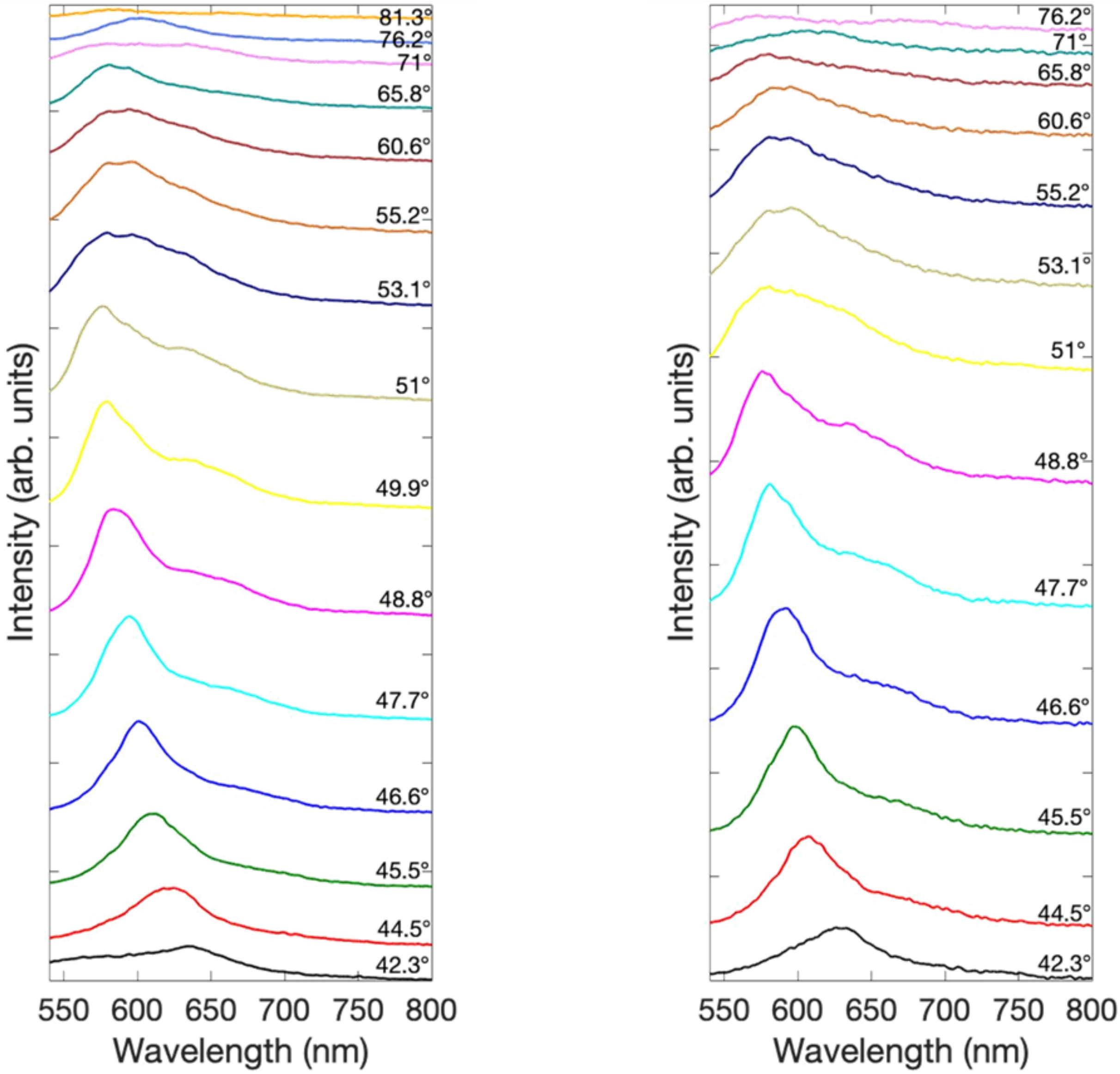

Figure S7. Effect of observation angle on the Ru probe coupled P-polarized emission spectra using KR excitation, 473 nm light excitation at 48° (left) and RK excitation at 180° (right).

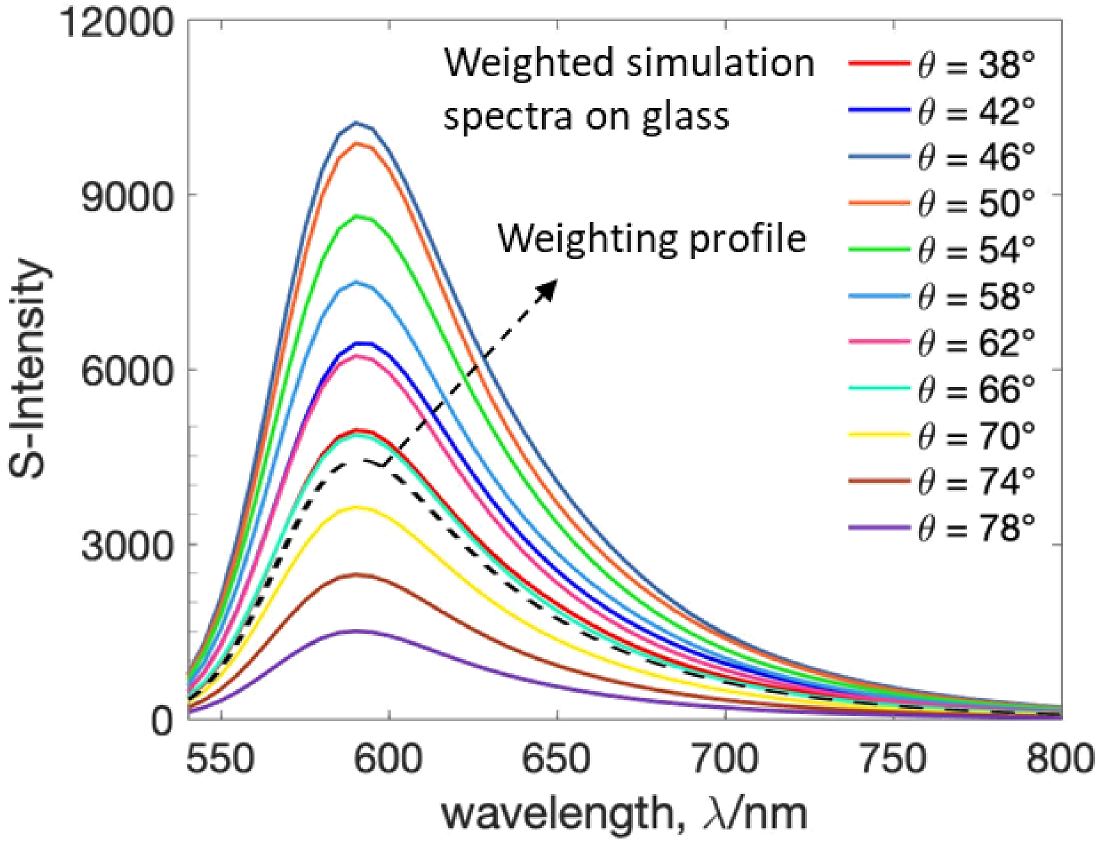

Figure S8. Simulated angular-dependent coupled emission spectra of one dipole source on glass. All spectra were weighted using the weighting profile (dashed line) based on Ru probe's intrinsic emission profile in Figure S3C.

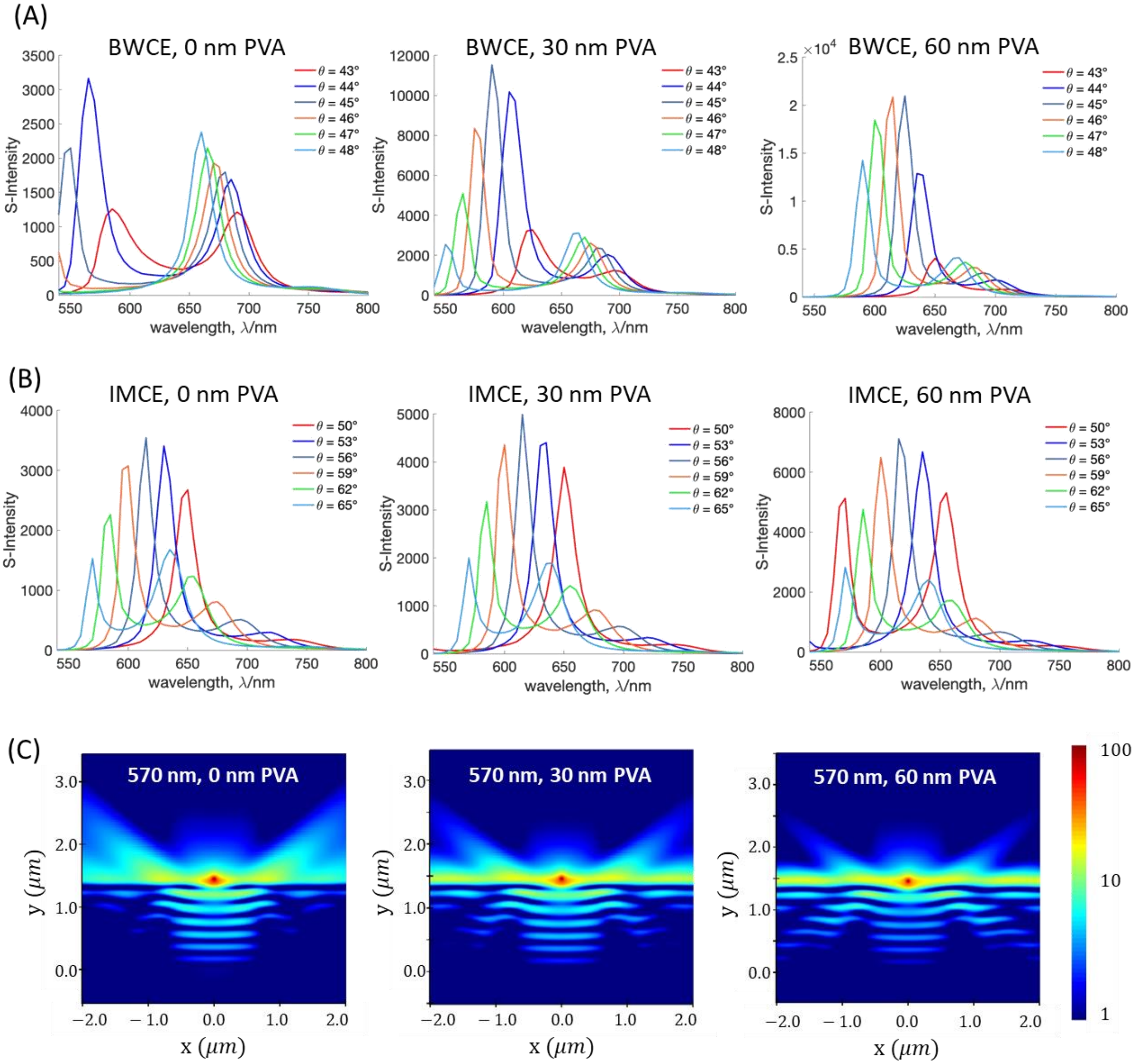

Figure S9. Effect of PVA thickness on dipole weighted S-polarized emission spectra in angular range of BWCE, Range 1, from 43 to 48°, (A) and IMCE, Range 2, from 50 to 65°, (B). Panel (C) shows the electric field distribution for 570 nm emission across the 1DPC structure, under a logarithmic scale from 1 to 100. PVA thicknesses are changing from left to right as 0 nm, 30 nm, and 60 nm.

Near-field movie – Single wavelength FDTD simulation model

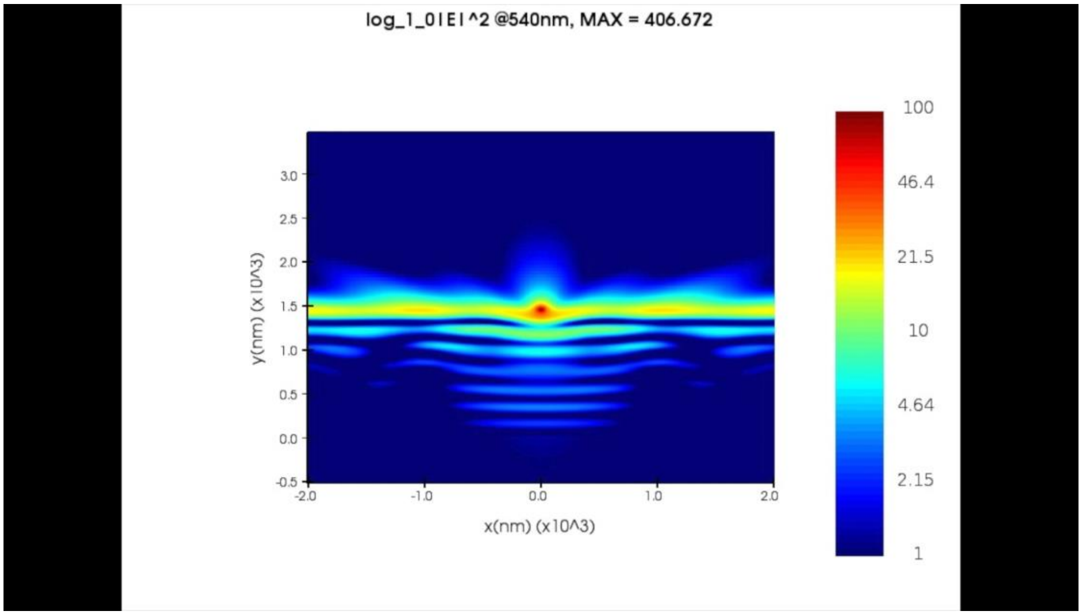

Figure S10. Movie showing evolution of wavelength-dependent field intensity distribution across 1DPC multi-layer structure. RK configuration. Wavelength increases from 540 nm to 800 nm with 10 nm increment. Logarithmic scaled color bar is from 1 to 100. Dipole source is in $\vec{Y}$-orientation.

Near-field movie – Single wavelength FDTD simulation model

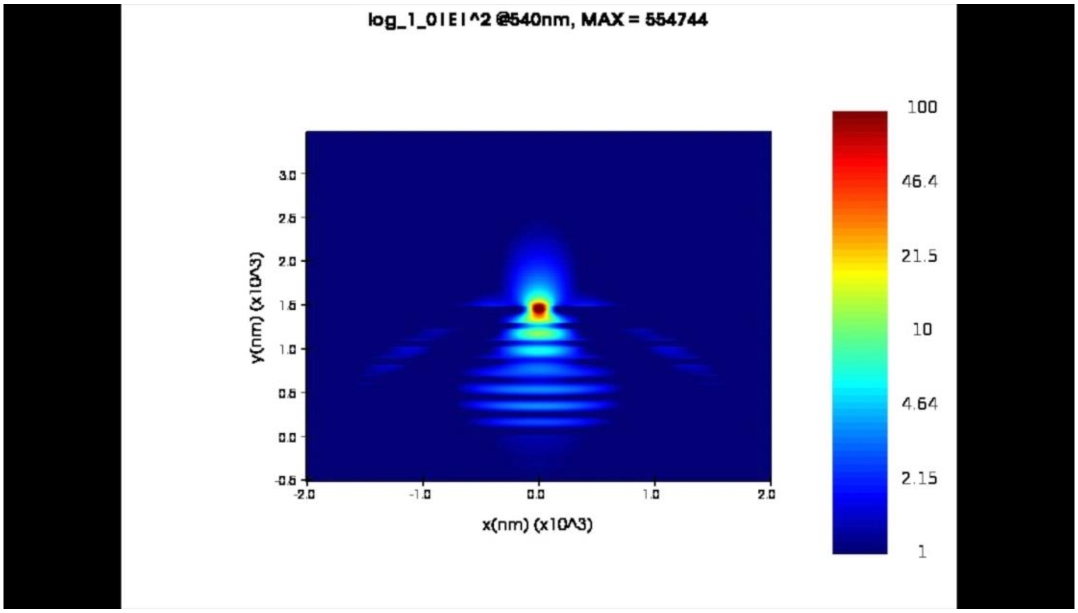

Figure S11. Movie showing evolution of wavelength-dependent field intensity distribution across 1DPC multi-layer structure. RK configuration. Wavelength increases from 540 nm to 800 nm with 10 nm increment. Logarithmic scaled color bar is from 1 to 100. Dipole source is in $\vec{X}$-orientation.

Near-field movie – Single wavelength FDTD simulation model

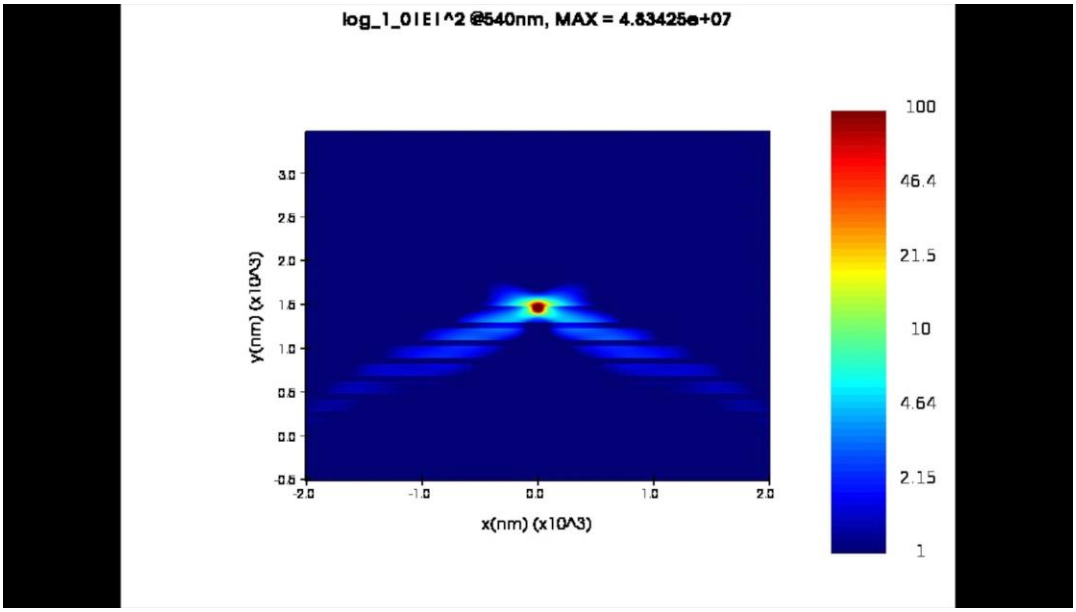

Figure S12. Movie showing evolution of wavelength-dependent field intensity distribution across 1DPC multi-layer structure. RK configuration. Wavelength increases from 540 nm to 800 nm with 10 nm increment. Logarithmic scaled color bar is from 1 to 100. Dipole source is in $\vec{Z}$-orientation.

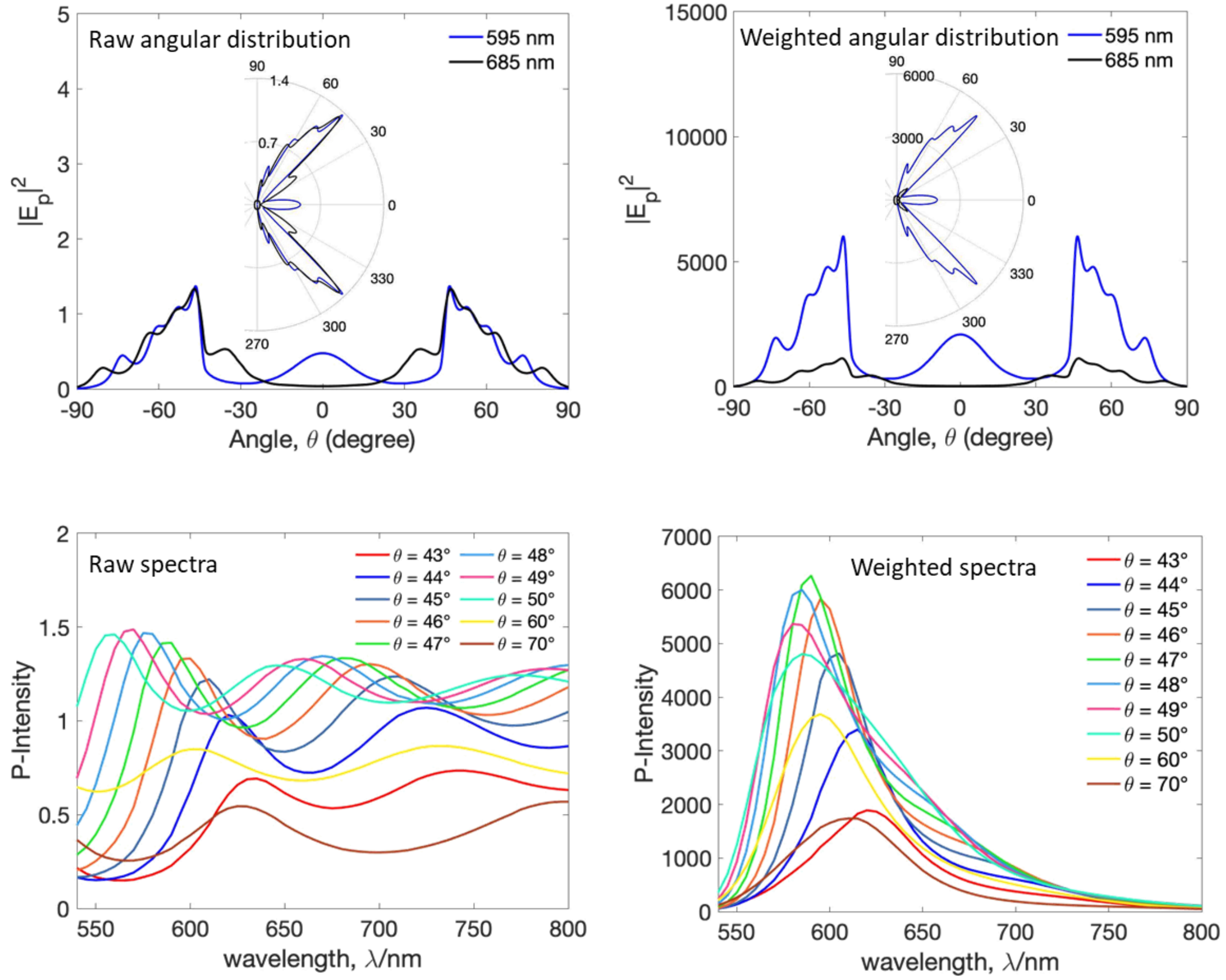

Figure S13. $\vec{X}$- and $\vec{Z}$- oriented single dipole on 1DPC simulation results in P-polarized emission. Top, angular distribution at selected wavelengths of 595 and 685 nm. Bottom, coupled emission spectra of selected angles from 43^{o} to 70^{o}. Raw results are shown on the left side, while weighted results are on the right side. Inset polar plots in the top panel are angular distribution of coupled emission across all angles from 270^{o} to 90^{o}.